

Evaluation of Heat Transfer Transport Coefficient for Cold Spray Through Computational Fluid Dynamics and Particle In-Flight Temperature Measurement Using a High-Speed IR Camera

A. Nastic¹ · B. Jodoin¹

Submitted: 20 August 2018 / in revised form: 16 October 2018 / Published online: 12 November 2018
© ASM International 2018

Abstract This work aims at obtaining experimental particle temperature readings during the cold spray (CS) process using a high-speed, high-definition infrared (IR) camera for multiple gas stagnation parameters to infer the suitability and accuracy of Nusselt number and drag coefficient correlations widely used in CS modeling. Measured particle temperatures are compared with values obtained through numerical modeling. Measured particle velocity using recorded data from the IR camera, based on particle streak and particle tracking velocimetry methods, is compared to values obtained from simulations. Additionally, particle velocities acquired using a Cold Spray Meter are also considered. Results demonstrate that only one of all common Nusselt correlations typically used in CS modeling results in accurate particle temperature predictions. Furthermore, the study shows that the drag coefficient correlation must incorporate the particle Mach number in order to provide acceptable particle velocity predictions.

Keywords cold spray · heat transfer transport coefficient · IR camera · particle temperature

List of symbols

Particle/gas interactions

a_1, a_2, a_3 Drag coefficient constants (–)
 A_p Particle cross-sectional area (m²)

A_{sp} Particle surface area (m²)
 C_1, C_2 Sutherland constants (kg/ms K^{1/2}), (K)
 c Gas local speed of sound (m/s)
 C_D Drag coefficient (–)
 $C_{p(g,f)}$ Gas specific heat at constant pressure evaluated at film temperature (kJ/kg K)
 $C_{p,g}$ Gas specific heat at constant pressure (kJ/kg K)
 $C_{p,w}$ Gas specific heat at constant pressure evaluated at particle surface temperature (kJ/kg K)
 C_p Particle specific heat at constant pressure (kJ/kg K)
 C_v Particle specific heat at constant volume (kJ/kg K)
 d_p Particle diameter (m)
 F_b Body force (N)
 $f_{\text{correction}}$ Nusselt number correction factor (–)
 \bar{h} Average convective heat transfer coefficient (W/m² K)
 k_B Boltzmann's constant (J/K)
 $k_{g,f}$ Gas thermal conductivity evaluated at film temperature (W/m K)
 K_n Knudson number (–)
 k_r Gas thermal conductivity evaluated at recovery temperature (W/m K)
 m_p Particle mass (kg)
 M_p Particle Mach number (–)
 \overline{Nu} Nusselt number (–)
 R_g Gas constant (J/kg K)
 Re_∞ Gas free stream Reynolds number (–)
 Re_p Particle Reynolds number (–)
 S_M Additional momentum source term (kg/m s)
 S_T Additional energy source term (J)
 T_f Film temperature (K)
 T_g Gas temperature (K)

✉ A. Nastic
Aleksandra.Nastic@uottawa.ca

¹ Cold Spray Research Laboratory, University of Ottawa, Ottawa, ON, Canada

T_p	Particle temperature (K)
T_r	Recovery temperature (K)
V_g	Gas velocity (m/s)
V_p	Particle velocity (m/s)
μ_g	Gas dynamic viscosity (Pa s)
$\mu_{g,f}$	Gas dynamic viscosity evaluated at film temperature (Pa s)
μ_w	Dynamic viscosity evaluated at particle surface temperature (Pa s)
ρ_g	Gas density (kg/m ³)
$\rho_{g,f}$	Gas density evaluated at film temperature (kg/m ³)
ρ_w	Gas density evaluated at particle surface temperature (kg/m ³)
Bi	Biot number (–)
d	Gas molecule diameter (m)
\mathcal{M}	Gas molecular weight (kg/mol)
\mathcal{N}	Number of gas molecules per mole constant (1/mol)
Pr	Prandtl number (–)
r	Recovery factor (–)
γ	Ratio of specific heats (–)

Radiation principles

C_3, C_4	First and second radiation constants (W m ²), (m K)
E_a	Emitted infrared energy by the atmosphere (W/m ²)
E_g^B	Radiation emitted from a blackbody at the surrounding temperature (W/m ²)
E_{mean}	Mean radiance emitted (W/m ²)
E_p^B	Radiation emitted by a blackbody at the particle temperature (W/m ²)
E_p	Emitted infrared radiation by the particle (W/m ²)
E_r	Emission of the surroundings reflected by the particle (W/m ²)
E_{ref}^B	Blackbody emitted energy at the atmospheric temperature (W/m ²)
$E_{\lambda b}$	Blackbody spectral emissive power (W/m ²)
$E_{\lambda p}$	Spectral electromagnetic radiation emitted by the particle (W/m ²)
W_{tot}	Total infrared radiation captured by the IR camera (W/m ²)
α_g	Surrounding gas transmittance (–)
ε_p	Particle emissivity (–)
$\varepsilon_{\lambda, T}$	Hemispherical spectral emissivity (–)
λ_1, λ_2	Specified wavelengths (μm)
$\tilde{\lambda}$	Intermediate wavelength (μm)
B, F, R	Plank's law parameters (–)
P	Gas static pressure (Pa)
T	Temperature (K)

t Time (s)

Introduction

Cold spray (CS) uses a converging/diverging nozzle to accelerate a gas (usually nitrogen, helium or air) to the supersonic regime (Ref 1). Metallic particles are injected in the flow and propelled to velocities ranging between 300 and 1200 m/s (Ref 2, 3). During their flight inside the nozzle, the particles also exchange energy with the propellant gas, resulting in particles having temperatures below their melting point throughout their flight (Ref 4, 5). Upon impact with the substrate, up to 90% of the in-flight particle's kinetic energy is converted into heat (Ref 6–8), while the remaining is converted into viscoelastic deformation and elastic energy. Substrate temperature and properties such as hardness and roughness can easily be measured/monitored, allowing for a direct observation/correlation of their influence on the deposition process. Accuracy of models simulating the heat transfer between substrate and gas flow has been validated by many using experimental data, which have led to understanding the contribution of substrate preheating on coating deposition processes (Ref 9–11). However, measuring the particle thermal state during its flight and upon impact proves to be technically challenging. Over the years, models have been developed and used to predict the gas flow and particles properties during the CS process (Ref 12–17). These models' accuracy is highly dependent on the assumptions made, which can lead to erroneous conclusions (Ref 18). As an example, the isentropic solution of the gas exit velocity at low stagnation pressure significantly deviates from results obtained through full Navier–Stokes viscous flow solutions as the losses through shocks and viscous effects are not included in the analysis as well as the effect of nozzle geometry (Ref 13, 18). While being a convenient tool for rough estimates, it is too simplistic to accurately describe and predict flow and consequently particle characteristics upon impact (Ref 19). Alkhimov et al. (Ref 20) presented a model which includes the presence of the bow shock at the substrate and the effects of nozzle boundary layer, showing the importance of considering both phenomena to forecast the particle properties at impact. Similarly, Kosarev et al. (Ref 21) developed an analytical model based on empirical equations to describe the gas flow using two-dimensional relations and including the outside supersonic jet flow structure, bow shock and heat transfer processes with the substrate. Despite providing a more realistic estimate of particle flow, both models use complex formulations, which makes them less versatile and reduces their practicality (Ref 18).

Consequently, to optimize accuracy of results, computational fluid dynamics (CFD) has become a widely used

approach to simulate the CS process. Results obtained through CFD such as gas flow pattern and particle velocity have shown good agreement with experimental data (Ref 22-25). Shock-wave structure visualization using Schlieren imaging (Ref 22) and particle velocity measurement using laser light sheet (Ref 24) and laser two-focus velocimetry (Ref 23) have been used to validate CFD results for flow structure and particle velocity.

However, a difficulty arises when trying to measure and model the in-flight particle temperature, required to fully describe the particle behavior. In the CS process, the particle temperature has only been reported on the foundation of theoretical analysis and CFD modeling, without any validation with experimental data. Lack of particle temperature measurement results from technological limitations due to the particle relatively low temperature and high velocity. In thermal spray processes, two-color optical pyrometry for in-flight particle temperature measurement has been used based on the Planck’s law of thermal radiation (Ref 26-30). The high thermal emission radiated by the particles heated to or near their melting point allows for suitable detection (Ref 31, 32). Recently, a one-color camera approach has also been developed to provide the radiation spectral analysis of in-flight particles with visual information of both the temperature and velocity distribution of particles within their trajectory in the thermal plasma spray plume (Ref 31). Spectroscopic techniques have also been used to identify and filter the thermal emission of particles in a plasma plume by collecting spectral signature signals of the plume alone (Ref 33). However, classical pyrometric particle temperature measurement can only provide information on particle temperature with reasonable precision above 1200 °C, which is by far superior to the CS stagnation parameters (Ref 34).

The lack of experimental data to support the CFD modeling of particle temperature challenges the reliability and accuracy of the heat transfer analysis and correlations currently used to describe the particle-gas interactions in CS processes. Nusselt number correlations frequently used in CS modeling lack validation for this specific flow configuration. Current calculations are made based on various theoretical assumptions from larger scale applications under different flow regimes. Multiple correlations to express the Nusselt number have been used in other fields to include the effect of either a large Reynolds number (Ref 35), high Mach number (Ref 36) or the boundary layer surrounding the particle periphery (Ref 37). To date, comparisons between existing Nusselt number correlations for CS processes have not been made due to the absence of experimental data required for proper validation.

The main goal of the current work is to initiate efforts to improve the understanding of particle heating process in

CS by focusing on the experimental measurement of particle temperature using a high-speed, high-definition infrared imaging technique. In-flight particle temperature measurements in the CS process have never been reported previously. Hence, assessment of such data, even in a limited set such as the one provided by this early initiative, will provide the ability to evaluate the accuracy of the currently used heat transfer correlations subsequently allowing a better understanding of the interactions between particle and gas flow in the CS process in general. To achieve this goal, an infrared camera operating in the mid-wave infrared (MWIR) spectral range (3-5 μm) is used to capture in-flight titanium particle temperature at the exit of a CS nozzle. The recorded data are also used to evaluate the in-flight particle velocity. Those measurements are used to assess the accuracy and precision of the Nusselt and drag correlations typically used in CS CFD studies.

Background

The particles motion and heat transfer processes are influenced by the flow-field characteristics, the particle drag, energy transfer coefficients and the particle properties. In analyzing micron-sized particles traveling conditions in supersonic CS flows, the inertial, rarefaction and compressibility effects must be considered.

Particle Motion

Particle acceleration is obtained by integrating the force balance equation acting on the particle;

$$m_p \frac{dV_p}{dt} = \frac{1}{2} C_D \rho_g A_p (V_g - V_p)^2 + F_b \tag{Eq 1}$$

where m_p , V_p , C_D , ρ_g , V_g , A_p and F_b are the particle mass, particle velocity, particle drag coefficient, gas density, gas velocity, particle cross-sectional area and body force, respectively. The body force can include gravity force (Ref 38), thermophoretic force (Ref 39), lift force (Ref 40), electrostatic force (Ref 38) and adverse pressure gradient from the shock wave (Ref 25).

The dependence of the drag resulting from pressure and viscous stresses applied at the particle surface on the magnitude of the particle relative velocity is expressed through the particle Reynolds number (Re_p);

$$Re_p = \frac{\rho_{g,f} |V_g - V_p| d_p}{\mu_{g,f}} = \frac{\text{Inertial forces}}{\text{Viscous forces}} \tag{Eq 2}$$

where μ_g is the gas dynamic viscosity and d_p is the particle diameter. The subscript f refers to the properties evaluated at the film temperature given by;

$$T_f = \frac{T_p + T_g}{2} \tag{Eq 3}$$

where T_p and T_g are the particle and gas temperatures, respectively.

Figure 1 shows the effect of increased inertial forces, i.e., increased Reynolds number, on the flow characteristics and the resulting drag coefficient, C_D .

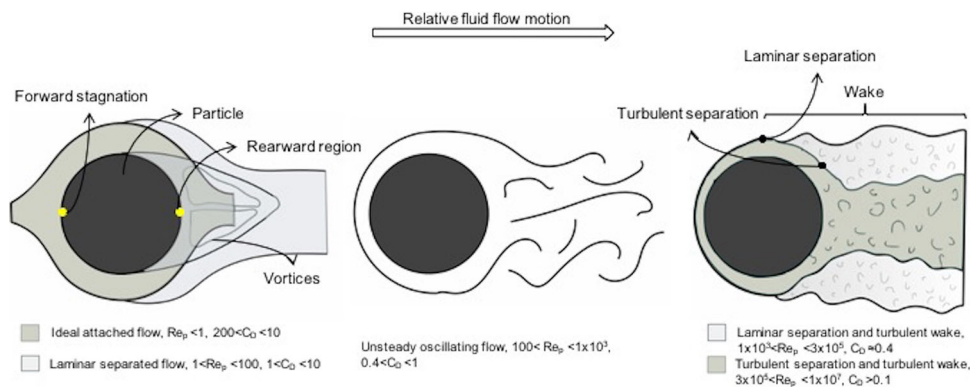
A symmetrical fully attached flow structure is encountered at low Re_p and C_D reaches values up to 200. The laminar symmetrical flow starts to separate from the particle surface as inertial forces increase. Vortices are subsequently generated, which create a lower pressure at the rearward particle zone. Further increase in Re_p leads to vortex shedding. Reynolds number from 1000 to a critical value of 3×10^5 introduces a turbulent wake zone with a laminar separation, which brings the C_D to a constant value of 0.4. Further increase in Re_p leads to a turbulent separation and the wake zone initiation location is moved rearward resulting in a decreased pressure and consequently a lower drag coefficient. This analysis is, however, limited to low-speed incompressible flows. A large number of studies in CS have used a $C_D = f(Re_p)$ to predict particle velocities (Ref 41-44). Others have, however, incorporated the influence of Mach number and compressibility effects (Ref 16, 45-47).

In particle laden flows, the presence of shock patterns near the particle surface resulting from compressibility effects can drastically affect the particle motion (Ref 48). In the current CS study, as particles are injected in the supersonic flow region, compressible effects are expected. The non-dimensional parameter controlling the compressibility factor is the particle Mach number, M_p , defined as;

$$M_p = \frac{|V_g - V_p|}{c} = \frac{|\Delta V|}{\sqrt{\gamma R_g T_g}} \tag{Eq 4}$$

where c is the gas local speed of sound, γ is the ratio of specific heats, $\gamma \equiv C_p/C_v$, R_g is the gas constant, and T_g is the local gas temperature. For $M_p \ll 1$, the flow is considered incompressible, while for Mach number above 0.6

Fig. 1 Illustration of flow characteristics around a spherical particle for increasing Re_p using stream structures. The variation of C_D is also provided. The fluid flows from left to right



significant effect of compressibility is expected (Ref 49). Figure 2 shows the variation of C_D with M_p for low and high Re_p .

For low Re_p , the drag coefficient uniformly decreases as a rarefied flow prevails (Fig. 2, line a). The occurrence of rarefaction is related to the Knudsen number, K_n , defined as;

$$K_n = \sqrt{\frac{\pi \gamma}{2}} \left(\frac{M_p}{Re_p} \right) = \frac{\lambda}{d_p} \tag{Eq 5}$$

where λ represents the mean free path of molecules. For continuum, conventional no-slip boundary condition is found for $K_n \leq 0.01$. In a non-continuum flow, partial-slip condition occurs and leads to three flow regime conditions: slip flow ($0.01 \leq K_n \leq 0.1$), transition flow ($0.1 \leq K_n \leq 10$) and free-molecular flow ($K_n \geq 10$) (Ref 50). Studies have shown that gas-particle interaction in rocket nozzles encounter all described flow regimes (Ref 36, 51, 52). As a result, all flow regimes are expected to occur in similar processes such as in the CS amid the use of a wide particle size range.

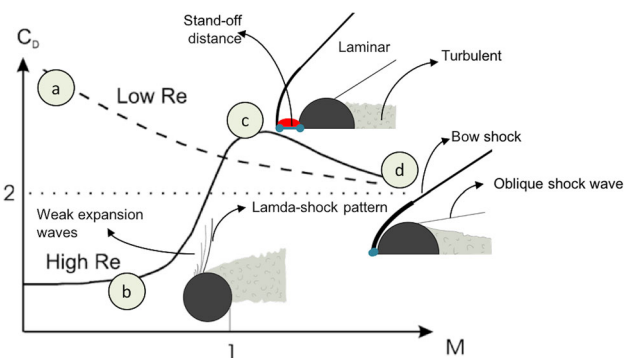


Fig. 2 Drag coefficient dependence on relative Mach number for low and high Re_p ($Re_p > 1.0 \times 10^4$). Insets illustrate the pressure flow structure around the particle for different M_p at high Re_p . The red zone shows the subsonic region created by the bow shock. The standoff distance between the shock and particle surface is also illustrated

As depicted in Fig. 2, at increasing M_p (near 1) and high Re_p , shock-wave structures appear. Weak expansion waves form at the particle surface followed by a lambda shock pattern, while the flow becomes locally supersonic. As a result of boundary layer/shock interactions, flow separation occurs earlier than for incompressible flows and the drag coefficient starts to increase (Fig. 2, point b). When a supersonic M_p is reached, a bow shock forms in front of the particle and the flow separation moves rearward: the drag coefficient increases and reaches a maximum value (Fig. 2, point c). Further increase in M_p brings the bow shock closer to the particle surface, and the following expansion wave further delays the flow separation process. Once the flow reaches the supersonic regime, it stabilizes as the previous general flow instabilities and shock initiations are reduced. Consequently, the drag coefficient decreases and eventually reaches a constant value of 2, unaffected by Re_p for $M_p > 1.5$ (Fig. 2, point d).

Multiple studies have been conducted to ensure that the drag coefficient gives proper representation of the flow field surrounding a particle (Ref 36, 52-56). As such, considerable collection of drag coefficient correlations is available in the literature. However, only a few rely on experimental data and are in a suitable form for computer programming/calculations. In the current study, the Henderson law is used to express the drag in the subsonic, transonic and supersonic relative flow as compressibility effects are of crucial importance in CS (Ref 18, 25, 53, 57, 58). It includes the continuum, slip, transition and molecular flow for M_p numbers up to 6 and for Re_p up to the laminar-turbulent transition. The effect of a temperature gradient on drag is also evaluated (Ref 53). Thermophoretic forces have been shown to arise at the particle surface from the temperature gradient in the continuous surrounding fluid and consequently the kinetic energy gradient from the surrounding molecules. Molecules found at the hot side of the gas are characterized by a higher collision rate than the ones located on the cold side, which results in a net force driving particles from hot to cold temperatures (Ref 50, 59). The Henderson drag coefficient is given as follows;

For $M_p \leq 1.0, C_{D1}$;

$$C_{D1} = 24 \left(Re_p + S \left(4.33 + \left(\frac{3.65 - 1.53 \frac{T_p}{T_g}}{1 + 0.353 \frac{T_p}{T_g}} \right) \times \exp \left(-0.247 \frac{Re_p}{S} \right) \right) \right)^{-1} + \exp \left(-\frac{0.5 M_p}{Re_p^{1/2}} \right) \left(\frac{4.5 + 0.38 (0.03 Re_p + 0.48 Re_p^{1/2})}{1 + 0.03 Re_p + 0.48 Re_p^{1/2}} + 0.1 M_p^2 + 0.2 M_p^8 \right) + 0.6 S \left(1 - \exp \left(-\frac{M_p}{Re_p} \right) \right) \tag{Eq 6}$$

For $1.0 < M_p < 1.75, C_{D2}$;

$$C_{D2} = C_{D1}(1.0, Re_p) + \frac{4}{3} (M_\infty - 1) (C_{D3}(1.75, Re_\infty) - C_{D1}(1.0, Re_p)) \tag{Eq 7}$$

For $M_p \geq 1.75, C_{D3}$;

$$C_{D3} = 0.9 + \frac{0.34}{M_\infty^2} + 1.86 \left(\frac{M_\infty}{Re_\infty} \right)^{1/2} \times \left(2 + \frac{2}{S_\infty^2} + \frac{1.058}{S_\infty} \left(\frac{T_p}{T_g} \right)^{1/2} - \frac{1}{S_\infty^4} \right) \times \left(1 + 1.86 \left(\frac{M_\infty}{Re_\infty} \right)^{1/2} \right)^{-1} \tag{Eq 8}$$

where $M_\infty = 1.75$, $C_{D1}(1.0, Re_p)$ and $C_{D2}(1.75, Re_\infty)$ represent the drag coefficient calculated using Eq 6 and 8, respectively, T_p is the temperature of the particle assumed isothermal, T_g is the temperature of the gas in the free stream, and S is the molecular speed ratio given by;

$$S = M_p \sqrt{\gamma/2} \tag{Eq 9}$$

In the current work, two other drag coefficients have been used and compared to results obtained from the Henderson correlation. Both of these drag coefficient correlations are used in CS applications to simulate particle velocity (Ref 40, 41, 44, 60, 61). The simplest form of drag coefficient expressed for spheres is defined by Schiller and Naumann (Ref 41) and given by;

$$C_D = \left\{ \begin{array}{ll} 0.44 & Re_p > 1000 \\ \frac{24}{Re_p} \left(1 + 0.15 Re_p^{0.687} \right) & Re_p \leq 1000 \end{array} \right\} \tag{Eq 10}$$

This relation accounts for any deviation from Stokes law at medium and high Reynolds numbers but disregards the effect of particle relative M_p .

The third evaluated drag model is the relation provided by Morsi and Alexander (Ref 40), which accounts for a particle Mach number greater than 0.4, given by;

$$C_D = a_1 + \frac{a_2}{Re_p} + \frac{a_3}{Re_p^2} \tag{Eq 11}$$

where the constants, given in Appendix A, apply for smooth spherical particles over a wide range of Re_p number.

Particle Heat Transfer

In transient particle heating encountered in the CS process, the Biot number (the ratio of external convective to internal conductance resistance to heat transfer) is calculated for spherical objects by (Ref 62);

$$Bi = \bar{h}(d_p/6)/k_p \quad (\text{Eq 12})$$

where \bar{h} and k_p are the average convective heat transfer coefficient and the thermal conductivity of the particle material, respectively. For Biot number values falling below 0.1, the temperature within the particle can be assumed uniform and the lumped capacitance method (LCM) can be used for the heat transfer analysis, as it has been done in some CS analyses (Ref 5, 57, 63–65). In the current work, the particle diameter is 150 μm and the particle (made of pure titanium) thermal conductivity only varies between 17 and 19.3 W/mK for temperatures between 27 and 727 $^\circ\text{C}$ (Ref 66). The approximate calculated average convective heat transfer coefficient using the Nusselt number correlations presented and described further in this section is in the order of 36×10^3 W/m²K. This leads to a Biot number smaller than 0.1. As such, the LCM is considered valid and the energy balance from the first law of thermodynamics yields;

$$m_p C_p \frac{dT_E}{dt} = A_{sp} \bar{h} (T_r - T_p) \quad (\text{Eq 13})$$

where m_p , C_p , A_{sp} and T_r are the particle mass, particle specific heat, particle surface area and the recovery temperature, respectively. The recovery temperature represents the gas temperature in the boundary layer surrounding the particle, which can be much higher than the free stream gas temperature due to the viscous heat dissipation effects when compressibility is not negligible (Ref 18, 57). The recovery temperature, T_r , is function of the particle Mach number and is expressed as follows;

$$T_r = T_g \left(1 + r \frac{\gamma - 1}{2} M_p^2 \right) \quad (\text{Eq 14})$$

where r is the recovery coefficient, close to 1 for gases (Ref 18). In the current study, as a laminar flow occurs at the particle front due to a Re_p close to 2000, the recovery factor is found to be expressed as (Ref 67, 68);

$$r = \sqrt{Pr} = \sqrt{\left(\frac{\mu_{g,f} C_{p(g,f)}}{k_{g,f}} \right)} \quad (\text{Eq 15})$$

The difficulty in predicting the particle temperature in the CS process resides in the uncertainty of evaluating the convection coefficient of the high-speed flow surrounding the particle. Commonly, \bar{h} has been calculated using the non-dimensional Nusselt number (\overline{Nu}), which represents the non-dimensional temperature gradient at the surface and is expressed as;

$$\overline{Nu} = \frac{\bar{h} d_p}{k_r} \quad (\text{Eq 16})$$

The gas thermal conductivity, k_r , is evaluated at the recovery temperature. The gas thermal conductivity is assumed to be only function of temperature and is given as follows (Ref 62);

$$k = \frac{9\gamma - 5}{4} \frac{C_v}{\pi d^2} \sqrt{\frac{\mathcal{M} k_B T_r}{\mathcal{N} \pi}} \quad (\text{Eq 17})$$

where $\mathcal{N} = 6.022 \times 10^{23}$ molecules/mole is the Avogadro's number, k_B is the Boltzmann's constant, $k_B = 1.381 \times 10^{-23}$ J/K, d is the gas molecule diameter, and \mathcal{M} is the molecular weight.

For forced flow over spherical particles, the Ranz and Marshall correlation (Ref 69) is expressed as:

$$\overline{Nu} = 2 + 0.6 Re_p^{0.5} Pr^{0.33} \quad (\text{Eq 18})$$

where Pr is the Prandtl number and is defined as the ratio of momentum diffusivity over thermal diffusivity. This correlation has been extensively used in the CS field (Ref 18, 41, 60, 70–73). However, it is very general in nature as it only expresses the effect of flow transition and separation encountered in incompressible flows (Ref 62). For a more accurate representation of particle heating experienced during CS, parameters such as the high particle Reynolds number (Ref 35), the boundary layer at the particle surface (Ref 37) and the high Mach number (Ref 36) must be considered in the calculation of the Nusselt number. Compressibility and rarefaction effects at the particle surface affect the flow boundary layer and consequently the heating processes (Ref 74). A few studies of particle traveling in the hot gas flow have used a correction factor along with Eq 18 to account for gas temperature variations in the boundary layer and the non-continuum effect. The correction factor is expressed as follows (Ref 37, 75–77);

$$f_{\text{correction}} = \left(\frac{C_{p,g}}{C_{p,w}} \right)^{0.38} \cdot \left(\frac{\rho_g \mu_g}{\rho_w \mu_w} \right)^{0.6} \quad (\text{Eq 19})$$

where C_p is the specific heat at constant pressure and the subscripts g and w refer to the gas and particle surface, respectively. The specific heat variation with temperature relation is taken as (Ref 78);

$$\overline{C_p} = 39.060 - 512.79\theta^{-1.5} + 1072.7\theta^{-2} - 820.40\theta^{-3} \quad (\text{Eq 20})$$

where $\theta = T(\text{K})/100$. The change in dynamic viscosity with temperature is expressed using the Sutherland two constant coefficients law given by;

$$\mu = \frac{C_1 T_f^{3/2}}{T_f + C_2} \tag{Eq 21}$$

where C_1 and C_2 are $1.663 \times 10^{-5} \text{kg/m s K}^{1/2}$ and 273.11 K, respectively. The density in the boundary layer corresponds to the gas density evaluated at the film temperature.

Other studies on CS particle temperature have included the Mach number effect on heat transfer. Multiple modified versions of the Nusselt expression given by Eq 18 exist, which introduce the effect of compressibility, such as;

$$\overline{Nu} = 2 + 0.44 Re_p^{0.5} Pr^{0.33} \exp(0.1 + 0.872 M_p) \tag{Eq 22}$$

valid only for $M_p > 0.24$ and when the gas temperature is larger than T_p (Ref 5). Another more general correlation that has been used in the CS field is expressed as (Ref 36, 57);

$$\overline{Nu} = \frac{2 + 0.459 Re_p^{0.55} Pr^{0.33}}{1 + \frac{3.42 M_p (2 + 0.459 Re_p^{0.55} Pr^{0.33})}{Re_p Pr}} \text{ for } M_p > 1$$

$$\overline{Nu} = 2 + 0.459 Re_p^{0.55} Pr^{0.33} \text{ for } 0 \leq M_p \leq 1 \tag{Eq 23}$$

where the gas thermal conductivity in the Prandtl number, k_g , is evaluated at the recovery temperature. These account for inertial and rarefaction effects by including both the continuum and transition region Nusselt number expressions.

Figure 3 summarizes the characteristics of the far-field flow, boundary layer and particle in reference to the presented equations. While multiple Nusselt number correlations have been used in CS for particle heat transfer description, lack of a more general correlation to account for all flow phenomena concurrently occurring at the particle surface is still missing. Moreover, as opposed to the case of the drag coefficient, it is yet to be determined if the accuracy of any of the available correlations is acceptable. The procedure described hereafter aims at evaluating these correlations using experimental validation for the CS process.

Experimental Setup

Powder Material

The feedstock powder used in the current study was a commercially pure gas atomized titanium powder with a 45 to 150 μm size (CP Ti Grade 1, Crucible Research, PA, USA). As the original powder exhibits a wide particle size range, the powder has been sieved to collect only particles in the range of 125 to 150 μm . Figure 4 shows the scanning electron microscope (SEM) images of the resulting sieved powder feedstock material, which displays a diameter size of $150 \pm 22 \mu\text{m}$ in average with small satellites attached at the particle surface. Due to the manufacturing process, the powder exhibits a spherical shape.

The selected particle diameter in this study has been chosen primarily to facilitate individual particle tracking during temperature readings. It is expected that larger particles with higher mass will travel at lower velocities in the flow (Ref 73) allowing ease of detection by the camera sensor. Studies have evaluated that the particle diameter has an effect on particle temperature and velocity, which consequently affects the coating quality (Ref 19, 79, 80). However, as the current study is not pursuing optimal coating deposition efficiencies or coating characteristics, decrease in particle velocity is of no concern but is rather sought. Additionally, despite having larger particle diameter than the typically sprayed powder size in CS applications (~ 1 to $100 \mu\text{m}$ (Ref 57, 79-81)), the flow physics and analysis procedure remain the same as the one presented in “Background” section as the particle diameter influence on the particle/gas interaction is scaled through the non-dimensional factors such as M_p , Re_p and K_n .

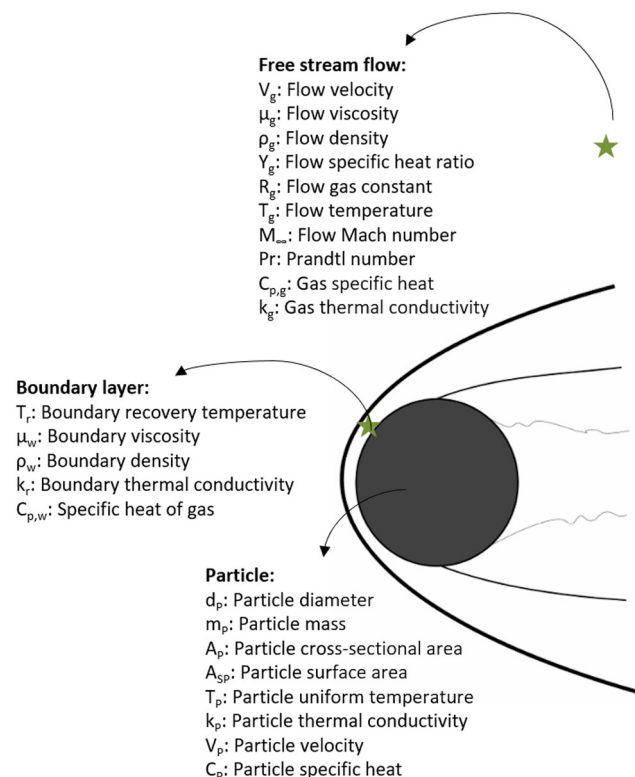


Fig. 3 Illustration of particle and surrounding flow characteristics used to solve the particle heat transfer and motion analysis

Fig. 4 (a) Sieved spherical titanium powder with final uniform diameter of 150 μm and (b) arrows pointing to satellites

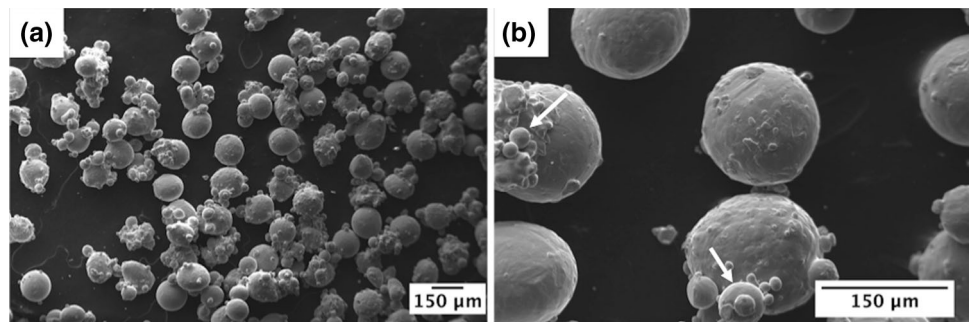


Table 1 Cold spray parameters

Parameters	Test 1	Test 2	Test 3
Gas temperature, °C	200	400	500
Gas pressure, MPa	0.69	0.69	0.69

Cold Spray Details

The cold spraying process was performed with the commercially available EP Series SST Cold Spray System (Centerline (Windsor) Ltd., Windsor, Ontario, Canada). The system runs using a 15-kW heater that can provide a maximum temperature of 650 °C and a maximum operating pressure of 3.45 MPa. A de Laval steel nozzle with a throat diameter of 2 mm and a divergent section length and exit diameter of 120 mm and 6.6 mm, respectively, was used for the current work. The sieved feedstock powder was fed using a commercially available AT-1200HP powder feeder (Thermach Inc., Appleton, WI, USA). The powder feed rate used was limited between 5 g/min to 8 g/min, to reduce the interaction between particles in the flow and facilitate individual particle tracking. All tests were performed without the presence of a substrate. Table 1 presents the stagnation pressures and temperatures for which the particles in-flight temperatures were measured. Nitrogen has been used as the propellant gas for all tests.

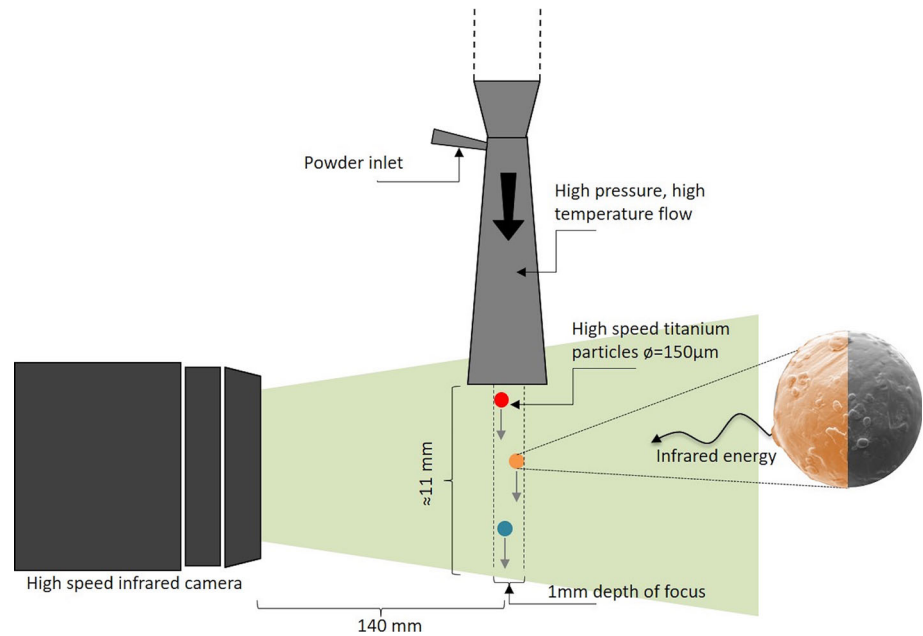
To ensure proper particle detection and temperature visualization during the single frame exposure time duration, the particle velocity was reduced to an appropriate level while maintaining high gas temperature to maximize particle heating. To reduce gas exit speed and consequently decrease particle velocity while maintaining a high stagnation temperature and supersonic conditions in part of the nozzle flow, the stagnation pressure was lowered down to 0.69 MPa. As a result, nozzle internal shockwaves are expected to occur, allowing the Mach number and gas velocity to decrease and the temperature to increase prior to the exit (Ref 13). This ensures that the testing conditions encompass as many flow regimes as possible to evaluate the correlations performance throughout these regimes.

Stagnation temperature was varied, as shown in Table 1, to obtain particle temperature difference with inlet operating gas temperature. As stated previously, these CS parameters are expected to generate low titanium coating quality as they are far from being optimal for coating production (Ref 4). However, the current study focuses on understanding heat transfer fundamentals at the particle level and obtaining particle temperature readings for model validation, which requires the chosen low spray parameters. Increasing the spray parameters to optimal values would not alter the heat transfer and momentum processes; therefore, the approach of the current study remains valid to the general CS deposition window.

Infrared Camera Setup

In order to measure the in-flight particle temperature as it travels in the flow outside the nozzle, a FAST M2 k high-speed camera has been used (FAST M2 k, Telops, QC, CA). The camera is equipped with an indium antimonide (InSb) MW detector and a narrowband cooled filter. A real-time temperature calibration (RTTC) technique is used as a calibration method. The approach is based on the detected characteristic fluxes ($\text{DL}/\mu\text{s}$ units) instead of the in-band radiance or observation of the variation in digital levels and blackbody comparisons used in common calibration techniques (Ref 82). The main advantage of the current calibration method is that it allows taking the integration time implicitly into account, which reduces the quantity of calibration data needed to be stored and acquired. Indeed, with traditional calibration methods, the radiometric characterization is applied using high-accuracy blackbodies over a range of temperature of interest and for all required exposure times, while in the current case, the fluxes represent the sensitivity of the camera readings with respect to the used exposure time. When applying this calibration method, the counts are first converted mathematically into fluxes, which consists of subtracting any count offsets related to circuitry readout present even at zero scene radiance and dividing by the exposure time. The RTTC method can also be applied to nonlinearly increasing detector-counts with integration time by proper modeling

Fig. 5 Cold spray of titanium particles and infrared imaging processes setup for particle surface temperature readings. The camera is positioned to frame both the nozzle exit area and in-flight particles



and parameterization. After the conversion to fluxes, all pixels are made equivalent by applying a pixel-wise offset and gain coefficients, which creates a single flux versus temperature relationship to be used for all pixels and all integration times. Hence, this calibration technique is also capable of adjusting to dynamically modified exposure times. The equations used to describe the instrument response, the radiometric gain and offset coefficients and the residual error can be found in the literature (Ref 82). Moreover, details on the steps required to implement the described calibration method are also provided in the study conducted by Tremblay et al. (Ref 82) and as such details are omitted here for conciseness.

The experimental setup and details are illustrated in Fig. 5. The camera has a $5 \mu\text{s}$ exposure time, which relates to the integration period used to capture a single frame of data. Its resolution was set to 320×16 window with pixel size of $55.6 \mu\text{m}$, which are non-optimal but still appropriate to capture and observe the microscale particles in-flight characteristics used in the current study. An acquisition rate of 24,000 frames per second was used to obtain sequences of the spray, which allowed capturing the thermal signature of fast moving particles. The working distance between the far end lens and the gas flow target, set at the center of the flow, was fixed to 140 mm to ensure proper analysis optical window size and resolution. The depth of field at the studied position was of 1 mm. The measurements obtained provide information about the particle mean surface temperature. The particle temperature in the gas flow was measured from the nozzle exit up to a standoff distance of approximately 11 mm. A statistical distribution of

temperature with respect to traveling distance was thus obtained. The IR camera provides a precision of $\pm 1 \text{ }^\circ\text{C}$ on temperature readings, which has been validated using a blackbody with a corresponding known emissivity of 0.99.

Individual particle in-flight velocity was also measured in the same range of distance from the nozzle exit. The velocity was obtained by means of two separate methods using the recorded IR camera imaging sequences. The first approach consisted of dividing the corresponding particle streak length by the exposure time as similarly accomplished in particle streak velocimetry (PSV) (Ref 83). The streak length is created by the frame superimposition on the image processor caused by particle movement within a single frame of time equal to the exposure time. In the current study, due to the limited powder feed rate, accurate streak lengths were obtained as particle streak overlapping was avoided. The second approach uses the particle position in sequential frames and the time between the corresponding frames to identify the resulting velocities, as analogously performed in particle tracking velocimetry (PTV) (Ref 83). Proper identification and tracking of the same particle need to be ensured between sequential frames in order to obtain the correct characteristic velocity. In the current study, only particles traveling straight within the flow were analyzed as their trajectory could easily be tracked, seen and predicted between frames.

Principles of Temperature Measurements

The radiation energy depends on the analyzed signal wavelength and the object temperature. The

electromagnetic radiation emitted by the particle, $E_{\lambda p}$, at a specific wavelength λ and temperature T , can be expressed using Planck's law;

$$E_{\lambda p}(\lambda, T) = \varepsilon_{\lambda, T} \frac{C_3}{\lambda^5 \left(e^{\frac{C_4}{\lambda T}} - 1 \right)} \quad (\text{Eq 24})$$

where C_3 and C_4 are the first and second radiation constants, respectively, given by;

$$\begin{aligned} C_3 &= 2\pi hc^2 = 3.741771 \times 10^{-16} \text{ Wm}^2 \\ C_4 &= \frac{hc}{k_B} = 1.438775 \times 10^{-2} \text{ mK} \end{aligned} \quad (\text{Eq 25})$$

where c is the velocity of light, h is Planck's constant, T is the particle temperature and k_B is the Boltzmann constant. The term $\varepsilon_{\lambda, T}$ is the hemispherical spectral emissivity defined as;

$$\varepsilon_{\lambda, T} = \frac{E_{\lambda p}(\lambda, T)}{E_{\lambda b}(\lambda, T)} \quad (\text{Eq 26})$$

where $E_{\lambda b}(\lambda, T)$ is the spectral emissive power of a blackbody at the evaluated wavelength and temperature. Moreover, since the used IR camera operates in a specific wavelength range of $\lambda_1 = 3$ and $\lambda_2 = 5 \mu\text{m}$, the mean radiance emitted by the particles between the given wavelength band is;

$$E_{\text{mean}} = \frac{1}{\lambda_2 - \lambda_1} \int_{\lambda_1}^{\lambda_2} E_{\lambda p}(\lambda, T) d\lambda \quad (\text{Eq 27})$$

Subsequently, as the radiance is continuous with wavelength and according to the intermediate theorem (Ref 84), the emitted energy can be expressed as;

$$E_{\text{mean}} = E_{\tilde{\lambda}} = \varepsilon_{\tilde{\lambda}, T} \frac{C_1}{\tilde{\lambda}^5 \left(e^{\frac{C_2}{\tilde{\lambda} T}} - 1 \right)} \quad (\text{Eq 28})$$

where $\tilde{\lambda}$ is between 3 and 5 μm .

The total infrared radiation, W_{tot} , captured by the IR camera comes from multiple sources, which include the emitted and reflected energy by in-flight particles as follows;

$$W_{\text{tot}} = E_p + E_r + E_a \quad (\text{Eq 29})$$

where E_p is the emitted infrared radiation by the particle, E_r is the emission of the surroundings that is reflected by the particle, and E_a is the emitted infrared energy by the atmosphere. The detected energy is integrated over Δt and at the wavelength band, $\tilde{\lambda}$, typical of the used sensor. In the MWIR spectral region, the atmospheric transmittance is of approximately 90% (Ref 85), which indicates a low absorptivity of incident radiation by the air particles. The diatomic nitrogen molecules are also transparent to the radiation (Ref 86). As a result, a higher radiation emission

is seen by the camera sensor from the analyzed object. Hence, the emission from the supersonic nitrogen flow at the nozzle exit, in which the particles are submerged, is also assumed to be transparent as the absorption is almost null at the CS working temperatures (Ref 87). Moreover, Eq 29 can be rewritten as;

$$W_{\text{tot}} = \varepsilon_p \alpha_g E_p^B + (1 - \varepsilon_p) \alpha_g E_{\text{ref}}^B + (1 - \alpha_g) E_g^B \quad (\text{Eq 30})$$

where α_g is the surrounding gas transmittance, ε_p is the particle emissivity, E_p^B is the radiation emitted by a blackbody at the particle temperature, T_p , E_{ref}^B is the blackbody emitted energy at the atmospheric temperature, and E_g^B corresponds to the radiation emitted from a blackbody at the surrounding temperature, T_g . These terms are also shown in Fig. 6 for the setup of the current study. For sake of clarity and simplicity, Eq 30 is presented such that it disregards the dependence from T and $\tilde{\lambda}$, although these have been taken into account. In addition, if the particles are treated as opaque gray bodies, their reflectivity is given by $\rho_p = (1 - \varepsilon_p)$. In summary, in Eq 30, the term $\varepsilon_p \alpha_g E_p^B$ expresses the emission from the particle captured by the IR camera detector, $(1 - \varepsilon_p) \alpha_g E_{\text{ref}}^B$ is the reflected emission by the particle surface from sources surrounding the particle for $(1 - \varepsilon_p)$ being the particle surface reflectivity, and finally $(1 - \alpha_g) E_g^B$ represents the emission from the atmosphere with $(1 - \alpha_g)$ representing the atmospheric emissivity. As noted earlier, since the atmospheric transmittance, α_g , is approximately 90%, the E_g^B has very little influence on the particle temperature measurement and as a result the entire atmospheric emission has been disregarded in the analysis. Consequently, combining Eq 28 and 30, a semi-empirical Planck's law adaptation with parameters R , B and F can be found to express the detected signal by the IR camera as follows (Ref 84, 88, 89);

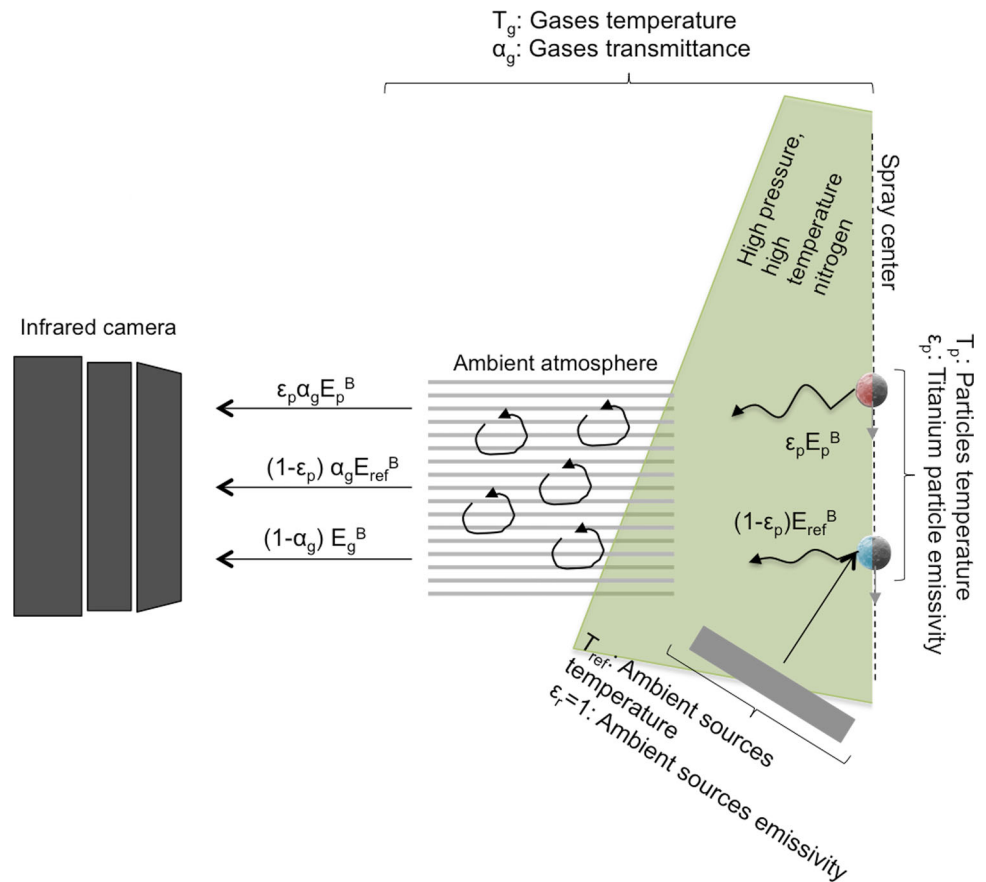
$$W_{\text{tot}} = \varepsilon_{\tilde{\lambda}, T_p} \frac{R}{\exp\left(\frac{B}{T_p}\right) - F} + \left(1 - \varepsilon_{\tilde{\lambda}, T_p}\right) \frac{R}{\exp\left(\frac{B}{T_{\text{ref}}}\right) - F} \quad (\text{Eq 31})$$

where R is function of the integration time and wavelength band, B is function of wavelength only and F is positive with a value close to 1.

Experimental Limitations

Based on the previous discussion on experimental setup and principles of particle temperature measurements, there are several fundamental limitations to successful particle temperature readings using the current high-speed IR camera. If the same optical window size and resolution are kept, a minimum powder size of 150 μm in diameter must

Fig. 6 Radiation received by the IR camera



be used to generate 3 pixels per particle and thus obtain a suitable surface temperature average. The current achievable acquisition rate limits a 150- μm particle velocity to about 225 m/s to ensure proper particle visualization between two consecutive frames. This maximal velocity value also includes the streak lengths that would be obtained during a 5 μs exposure time. Consequently, the CS parameters need to be adjusted to ensure such particle exit maximal velocity. Additionally, this analysis is easiest for spherical particles; however, if irregular particles are to be used, the irregularities must be larger than a pixel size to be visible. In terms of particle material, the limitations are mostly based on material/surface emissivity that must allow detection by the thermal camera sensor in the 3 to 5 μm wavelength range.

Particle Emissivity

The emissivity of pure titanium powder analyzed in the current study has been set to the absorptance, A , measured by Tolochko et al. for the same powder material and size (Ref 90-92). If it is assumed that all surrounding sources enclosing the analyzed particles are at the same temperature, T_{ref} , then based on Kirchhoff’s law, the emissivity and absorptivity of

the particles are equal in magnitude at any given temperature and wavelength (Ref 62). The absorptance is defined as the ratio of absorbed to incident radiation. Hence, Tolochko et al. have measured the absorptance of pure titanium powder to be 0.77 at a wavelength of 1.06 μm and decreases to 0.59 at a wavelength of 10.6 μm . A reasonable number of studies have measured the spectral emissivity of pure titanium material and oxidized titanium (Ref 93-98). All measured values of spectral emissivity show a slow decrease with increasing wavelength, in accordance with Tolochko et al. work, and a gradual increase with rising temperature, which is generally the rule by which metal emissivity abides (Ref 62, 99). As a linear trend is generally observed for pure titanium emissivity with wavelength up to 10.6 μm , an emissivity of 0.71 is calculated appropriate for the current study given the analyzed MWIR range and based on emissivity boundary values evaluated by Tolochko et al. (Ref 93, 98). In spite of the importance of powder emissivity value, the temperature measurement uncertainty due to powder emissivity value is decreased when the analyzed emitted radiation is reduced to shorter wavelengths (Ref 100). Consequently, any small deviation of emissivity from the chosen value in the current study is expected to result in minimal measured temperature variation.

Cold Spray Meter Setup

The in-flight particle velocity at a standoff distance of 5 mm from the nozzle exit, without the presence of a substrate, has also been measured using a Cold Spray Meter (CSM) eVolution (Tecnar Automation Ltd., St-Bruno, Canada). This technique is widely accepted and used for the measurement of particle velocity of various types and sizes (Ref 3, 25). A continuous laser with an 810 nm wavelength illuminates the particles during their flight. A dual-slit photomask captures the diffracted light from each individual particle as they pass in front of the sensor. The signature intensity of diffracted light from each particle is first amplified and filtered before being sent to an internal interpreting system. Subsequently, the velocity of particles is calculated internally by using the traveling distance and time interval between the two mask slits. The device is designed to output particle velocities ranging between 10 to 1200 m/s for particle diameters in the range of 5 to 300 μm . This measuring process has been operated for spray parameters used in Test 1 and Test 3 as they represent the lowest and highest spray parameters, respectively, as shown in Table 1. Consequently, obtained velocity results have been compared to those calculated using the infrared imaging techniques to verify the correctness of particle identification in the latter process and its accuracy. Moreover, the comparison is used to provide possible additional means of measuring particle velocity in CS processes.

CFD Details

Computational Domain

The commercially available Computational Fluid Dynamic (CFD) package ANSYS Fluent 18 software was used to model the gas and particle flow inside and outside the nozzle. A two-dimensional, axisymmetric model was used due to the symmetrical characteristic of the flow, and particles were injected at the symmetry line. Figure 7 shows the full assembly, which includes the nozzle with a

throat diameter of 2 mm, an exit diameter of 6.6 mm and a conically diverging length of 120 mm. The boundary conditions used in the current study are summarized in Table 2.

Domain Meshing

The computational domain of the 2D axisymmetric nozzle shown in Fig. 7 has been meshed using ANSYS WB Meshing Tool. The domain has been discretized into separate grids, and edge sizing was used to simplify the control of the meshing process. A structured quadrilateral non-uniform mesh was used, as shown in Fig. 8, as it provides a larger convergence capability. A biased 1.2 growth rate was used on vertical edges to provide higher precision and resolution near the walls.

The selected grid meshing consists of 486,275 elements with mesh quality of minimal orthogonal quality equal to 0.7 and maximum aspect ratio of 30. The grid density allows good accuracy in regions of complex flow phenomenon. The solution is iterated until convergence is reached by demonstrating first a decrease in residuals by at least three orders of magnitude and then by ensuring that the net mass and energy imbalances are below 0.01%.

Governing Equations

Gas Flow

The Navier–Stokes equations for compressible flows have been used to solve the gas stream motion. Mass, momentum and energy conservation have been used as governing equations as follows;

$$\frac{\partial \rho}{\partial t} + \frac{\partial}{\partial x_i} (\rho u_i) = 0 \quad (\text{Eq 32})$$

$$\frac{\partial}{\partial t} (\rho u_i) + \frac{\partial}{\partial x_j} (\rho u_i u_j) = \frac{\partial}{\partial x_j} \left[-P \delta_{ij} + \mu \left(\frac{\partial u_i}{\partial x_j} + \frac{\partial u_j}{\partial x_i} \right) \right] + S_M \quad (\text{Eq 33})$$

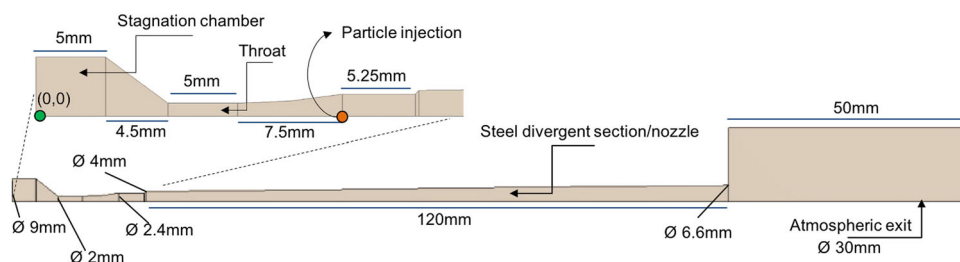
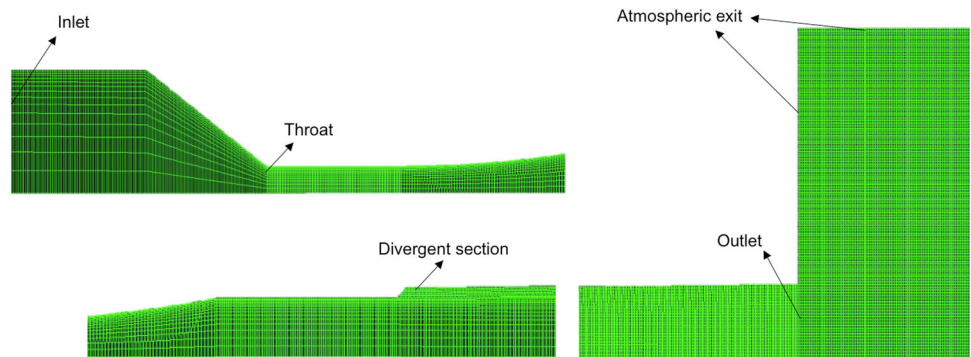


Fig. 7 Computational domain dimensions. The stagnation chamber, converging section and throat are magnified for clarity. Particle downstream injection location on the x-axis is provided in orange, and upstream injection is shown at a (0,0) position in green (Color figure online)

Table 2 Boundary conditions

Location	P	v	T
Nozzle inlet	Specified stagnation	$\frac{\partial v}{\partial n} = 0$	Specified stagnation
Surrounding atmosphere	Ambient condition	$\frac{\partial v}{\partial n} = 0$	$\frac{\partial T}{\partial n} = 0$
Nozzle walls	$\frac{\partial P}{\partial n} = 0$	0	$\frac{\partial T}{\partial n} = 0$
Symmetrical axis	$\frac{\partial P}{\partial r} = 0$	$\frac{\partial v}{\partial r} = 0$	$\frac{\partial T}{\partial r} = 0$

Fig. 8 Domain meshing details



$$\frac{\partial}{\partial t} (\rho C_p T) + \frac{\partial}{\partial x_j} (\rho u_j C_p T) = \frac{\partial}{\partial x_j} \left(\lambda \frac{\partial T}{\partial x_j} \right) + S_T \quad (\text{Eq 34})$$

where, t , P , C_p , u_i , μ , S_M and S_T are the time, gas static pressure, specific heat at constant pressure, gas velocity components, dynamic viscosity, additional source terms in momentum and energy equation, respectively. The additional terms (S_M and S_T) have been neglected since low powder feed rates have been used. These terms are disregarded for high Stokes number, St , and low momentum interaction parameter Π_{mom} (Ref 39). In the current study, given the low particle flow rate, in which the injected particles represent only a minor volume fraction within the nitrogen medium, it is reasonable to assume lack of particle–particle interaction. Hence, the particle phase has been simulated through a Lagrangian process as an inert point in space. Similarly, the gas phase momentum is not affected by the presence of particles due to the very small particle loading encountered in the current study and commonly in general CS applications. A pressure-based solver with a Green-Gauss node-based gradient method has been used to simulate the nitrogen flow. In addition, a second-order accuracy spatial discretization was used to model the pressure while a QUICK scheme has been set to solve the density and momentum equations.

Gas Properties Hypotheses

To account for compressibility effects, the ideal gas law is used. The compressibility factor of nitrogen for pressures and temperatures up to 10 MPa and 627 °C, respectively,

exhibit only a deviation of less than 4%, which supports the use of the ideal gas assumption (Ref 78). A two-coefficient temperature-dependent Sutherland law is used to account for viscosity variation with temperature, which has been demonstrated to be important in high-speed compressible flows (Ref 46, 63).

Turbulence Model

Due to the high velocity of the supersonic flow, inertia forces are expected to dominate the viscous dissipation effects, which would lead to a high resulting Reynolds number. As a consequence, the flow was assumed to be turbulent. Most turbulence models used to simulate the gas flow in the CS process are based on the closure of the Reynolds Averaged Navier–Stokes (RANS) equations. Models such as the standard $k-\epsilon$ (Ref 24, 57), the RNG $k-\epsilon$ (Ref 13, 45, 58), the realizable $k-\epsilon$ (Ref 25), the RSM, the SST k (Ref 22), the Spalart–Allmaras (Ref 14), the compressibility modified $k-\epsilon$ (Ref 44), the thermally modified $k-\epsilon$ (Ref 41, 101) and the multi-phase modified $k-\epsilon$ (Ref 102) have been used in the simulation of the CS process. In the current study, the RNG $k-\epsilon$ model has been chosen, as it has proven to significantly improve accuracy and precision in calculating the flow structure (Ref 18).

Discrete Phase Coupling

The titanium particle phase was injected in the nozzle domain near the throat section, as illustrated in Fig. 7, parallel to the CS flow stream. The forces and heat transfer

Table 3 Simulated phases properties

Property	Nitrogen flow	Titanium particle ($\varnothing = 150 \mu\text{m}$)	Copper particle ($\varnothing = 15 \mu\text{m}$)
CS parameters	N/A	0.69 MPa, 200 °C/400 °C/500 °C	3.45 MPa, 650 °C
Injection location	N/A	Downstream	Downstream and upstream
Density, kg/m^3	Ideal gas	4850	8978
Specific heat capacity, J/kg K	1040.67	544.25	381
Thermal conductivity, W/mK	0.0242	18	387.6
Viscosity, kg/ms	Sutherland law	N/A	N/A
Initial velocity, m/s	0.1	0	0
Initial temperature, °C	25	25	25

from the continuum applied to the particle surface were calculated using Newton's balance equation and the lumped capacitance method as described in "Background" section. The drag coefficients expressed using Eq 10 and 11 have been selected within the Fluent software interface. However, the drag equation described using Eq 6 to 9 has been separately programmed using C language through Visual Studio, subsequently compiled in Fluent solver and attached as a user-defined function. Similarly, the entire heat transfer analysis, described by Eq 12 up to Eq 23, has been written in C programming language and dynamically loaded as a build in user-defined function. Table 3 presents the material properties used to simulate the experimentally conducted downstream injection spray of the titanium particles. A one-way coupled Lagrangian approach was chosen to solve the particle-related equations based on the local gas properties.

In addition to the titanium particle downstream injection model, two additional simulations have been performed. Both have been conducted using regular spray parameters consisting of high inlet stagnation pressure and temperature of 3.45 MPa and 650 °C as well as common powder particle size and material used in the CS community to obtain proper particle deposition. The injection of a single 15 μm copper particle was first made downstream, at the location illustrated in Fig. 7, and the second simulation was conducted for upstream injection at the domain inlet. The copper particle material and size have been selected as they are most widely used in the CS field. The material properties for all simulations as well as details of spray parameters and powder injection location are given in Table 3. The copper particle velocity has been simulated using all three presented drag coefficients using Eq 6 to 9, Eq 10 and 11. Similarly, to obtain in-flight particle resulting temperature, all four Nusselt expressions have been tested (Eq 18, 19, 22 and 23).

The main purpose of the high spray parameters simulations is to evaluate the temperature error caused if less accurate correlations are used for a high deposition CS

parameter process. Although the correct and most accurate correlations have already been found with the conducted tests using large titanium particles, the significance of the error encountered during high deposition spray parameters is of utmost relevance for a wide range of applications and thus its evaluation is crucial.

Results and Discussion

CFD General Flow

Figure 9 shows the gas temperature and velocity contours in the converging/diverging nozzle and nozzle exit vicinity section for stagnation temperature conditions presented in Table 1. When the inlet stagnation temperature is 200 °C, the maximal gas temperature and velocity reached within the diverging nozzle section correspond to 187 °C and 827 m/s, respectively. The lowest temperature of -129 °C is reached 0.0285 m after the throat in the supersonic region at a flow Mach number of 3.33. For the case of an inlet stagnation temperature of 400 °C, the maximal temperature and velocity of the gas in the diverging section are 377 °C and 985 m/s, respectively. At 0.0285 m, the temperature reaches only -66 °C at a region with a Mach number of 3.37. Similarly, for the case of a 500 °C inlet temperature, the gas reaches 477 °C and 1060 m/s in the diverging section of the nozzle. The lowest temperature after the throat reaches -35 °C at a flow Mach number of 3.36.

The model also predicts the occurrence of a shock train initiated approximately 70.75 mm from the powder inlet location. Once the flow is at $M = 2.5$, the acceleration process is suddenly interrupted. As the pressure ratio is much lower than the pressure ratio for which the nozzle is designed, a shock wave is induced (with reflections also being generated) to reach and recover the ambient pressure at the nozzle exit. This occurrence is the main advantage of utilizing low inlet stagnation pressure as it forces particles

Fig. 9 2D axisymmetric model of nitrogen flow velocity (bottom) and temperature (top) contours in the diverging/converging section and atmospheric outlet for an inlet pressure of 0.69 MPa and gas stagnation temperature of (a) 200 °C, (b) 400 °C and (c) 500 °C

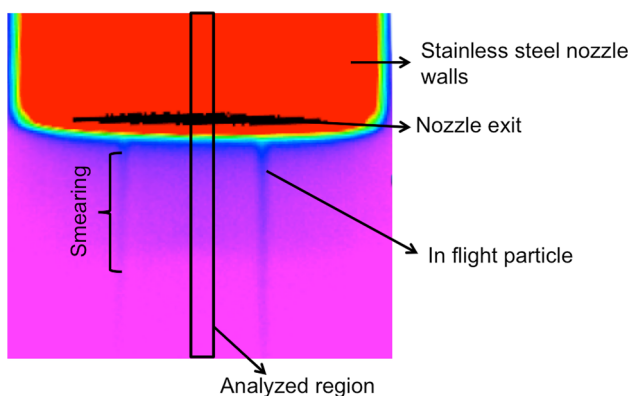
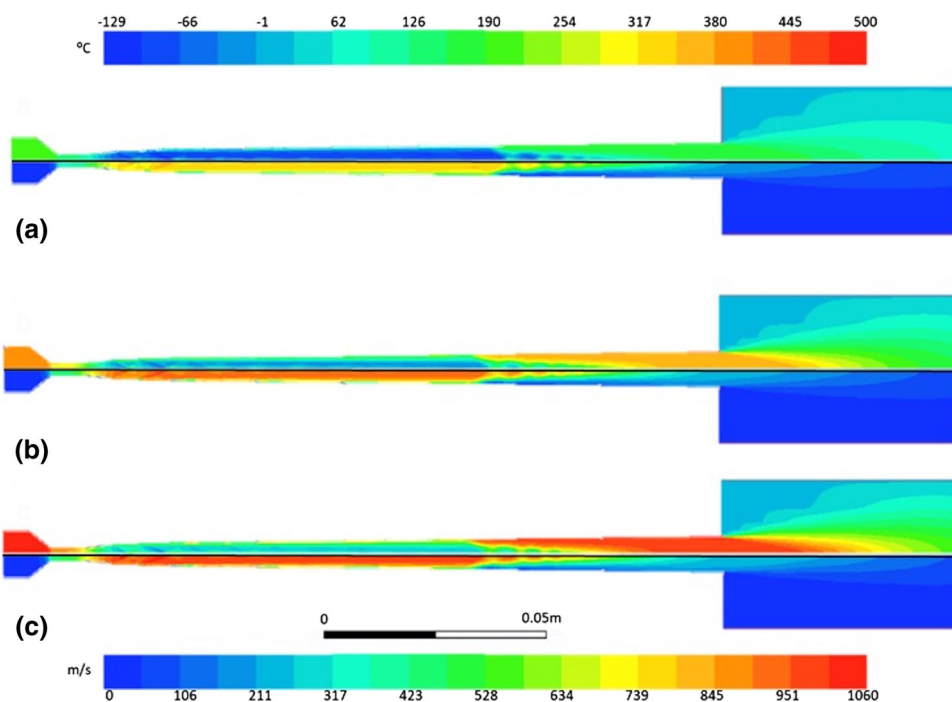


Fig. 10 Large IR camera view of the entire nozzle and in-flight particles exiting during spray showing the testing setup. For particle velocity and temperature measurements, the IR camera has been set to only view and analyze the region delineated by the rectangle

to heat up and slow down prior to the exit, which is crucial for the current study to cover all complex flow regimes encountered in CS.

Particle Velocity

Experimental Measurements

Figure 10 gives details of the analyzed region for particle temperature and velocity measurements. The shown zone has been taken with an exposure time of 50 μs, in which

two particles are seen to exit the nozzle. The IR camera view for subsequent particle characteristics measurements (temperature and velocity) is delineated by the rectangular shape. As mentioned previously, during particle velocity and temperature readings, a section of the nozzle and the exit particle laden flow are both seen by the IR sensor.

The individual particle velocity measurement procedure using the particle visualization across two subsequent frames in the analyzed region, at different stagnation temperatures, is shown in Figure 11. The analyzed region is 17.74 mm by 0.83 mm, which includes 6.62 mm of nozzle length and 11.12 mm of nitrogen particle laden flow length outside the nozzle, as depicted also in Figure 10. Particle shape and position are easily discernable and position readings have been made either at the particle rear end or front surface. The time interval between two successive frames corresponds to 41.5 μs.

Results indicate particle velocity of 175 ± 28 , 179 ± 17 and 194 ± 16 m/s for gas stagnation temperatures of 200, 400 and 500 °C, respectively. As seen, the measurements have been taken for particles without or slight trajectory deviations in the flow, which renders the particle velocity readings between subsequent frames possible and accurate. Moreover, the obtained images confirm low particle feeding rate required to have low particle loading effect on the gas flow. A low particle density in the flow along with short duration time between two images is needed for this method to accurately provide

Fig. 11 Particle velocity measurement using the PTV procedure between two consecutive frames for stagnation gas temperature of (a) 200 °C, (b) 400 °C and (c) 500 °C. Results indicate a velocity of (a) 172 m/s, (b) 176 m/s and (c) 184 m/s for the illustrated particles. A scale is provided at the top left corner

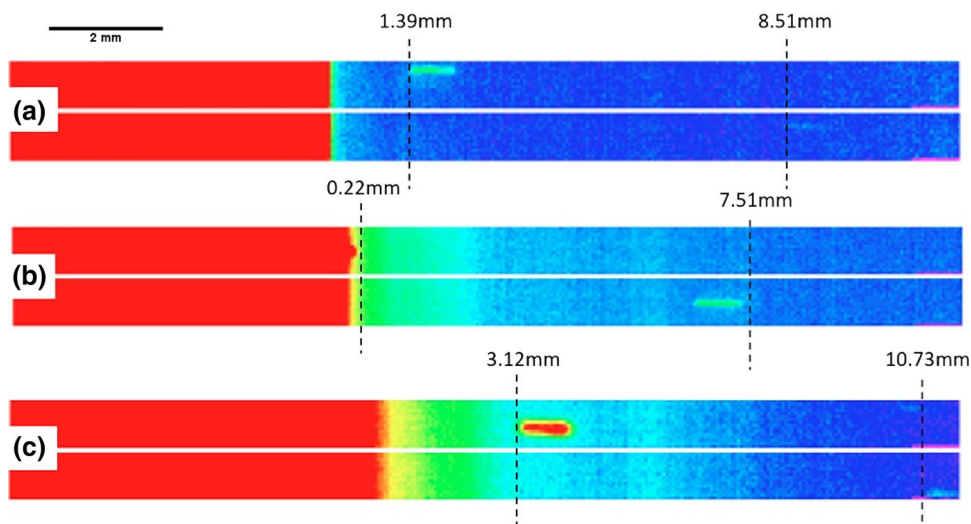
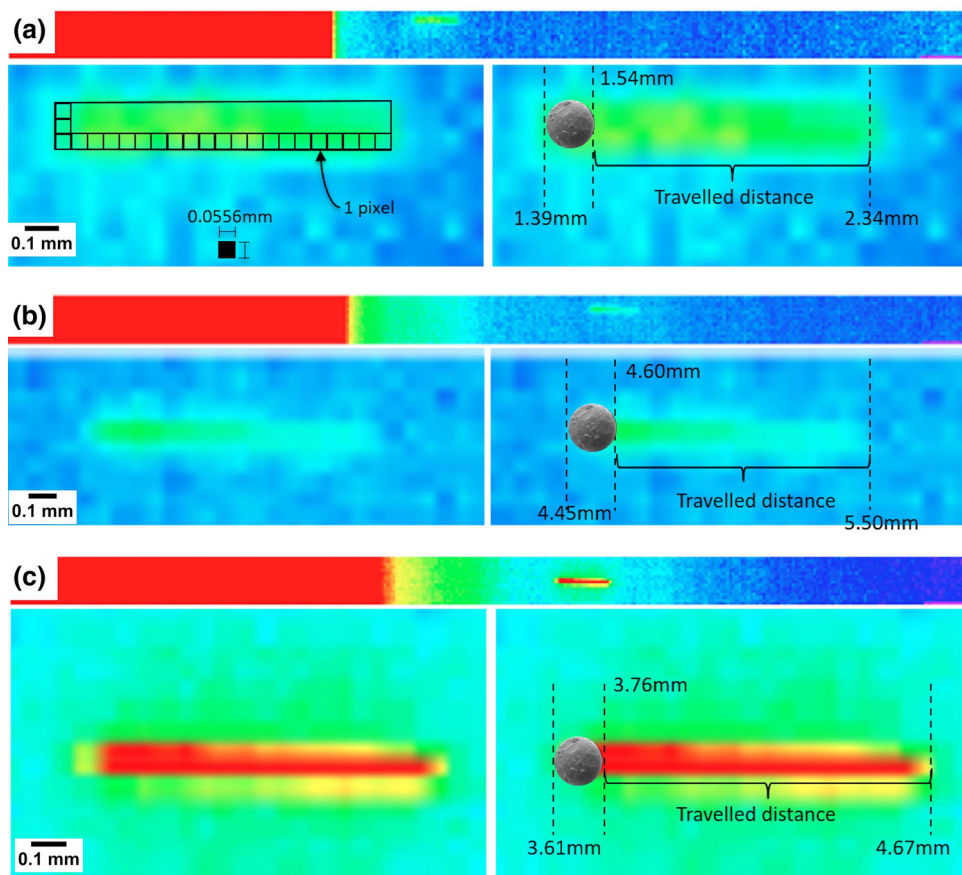


Fig. 12 Particle velocity measurement using the PSV procedure obtained under a 5 μ s exposure time for stagnation gas temperature of (a) 200 °C, (b) 400 °C and (c) 500 °C. Results indicate a velocity of (a) 160 m/s, (b) 180 m/s and (c) 182 m/s for the illustrated particles. A particle diameter of 150 μ m was assumed. The pixel size and resulting error that can occur in measurement due to the pixel resolution is also illustrated in (a)



velocity measurements. Results show that the large titanium particles reach higher kinetic energy at higher stagnation temperatures, which is in accordance with gas dynamic principles.

Figure 12 shows the results of particle velocity measurement through streak analysis. In contrast to the PTV method, the PSV is capable of providing velocity data as a

function of distance from nozzle exit as the streak length is measured locally. Results indicate a velocity of 153 ± 27 , 169 ± 26 and 183 ± 47 m/s for gas stagnation temperatures of 200, 400 and 500 °C, respectively. Additionally, measurements show that the velocity within a distance of approximately 11 mm from the nozzle exit is kept constant across the spray plume for all three tested stagnation

temperatures. A particle diameter of 150 μm was used for the calculations, which can lead to minor deviations in PSV measurements as the actual diameter might slightly differ from the average. Moreover, increased particle blurriness based on the particle pixel definition can also lead to small errors.

The particle velocities measured through the CSM, the PTV and PSV method using the IR camera, from the nozzle exit up to 11 mm downstream, are compared in Fig. 13 for the cases of stagnation temperatures of 200 and 500 °C. The results are represented using a box and whisker plot. A large range in velocities is observed for results obtained using the CSM, which is mainly associated with the broadness of the analyzed region. Slower particles found at the flow boundaries and smaller faster particles located in the center of the stream are both detected by the CSM while they are outside of the IR scope and its associated depth of focus. Although results obtained using the CSM show a large scatter, the median correlated with the average size particle velocities is compared with the PTV and PSV methods for future correlations with CFD results. At a gas stagnation of 200 °C, the particle average velocity is measured to be 183 ± 32 , 164 ± 24 and 153 ± 27 m/s when measured using the CSM, IR PTV and IR PSV methods, respectively. At 500 °C, the average reaches 195 ± 54 , 177 ± 17 and 169 ± 31 m/s under the analysis using the CSM, IR PTV and IR PSV, respectively.

Particle speeds obtained through the PSV method at both stagnation temperatures show the largest decline in median values when compared to the velocities obtained

using the CSM and PTV technique. An approximate difference of 36 and 23 m/s occurs between the average for particles traveling in a gas of 200 and 500 °C stagnation temperatures, respectively. All three techniques include an uncertainty related to the measurement process principle they use. Both the CSM and PTV methods rely on the measurement of particle distance traveled within the flow under a specific time. Consequently, both methods include, although being very small, intrinsic errors associated with particle path deviation. The CSM includes a pattern recognition analysis that allows only particles that deviate from their traveling path by an angle less than 10° to be properly detected, which provides increased particle velocity measurement accuracy. Similarly, due to the visual aspect of the PTV velocity evaluation process, particle with perceivable angular position can be eliminated from the analysis. In addition, the PTV process includes some uncertainty arising from the difficulty of assuring that the same particle is being tracked between subsequent measuring steps, which could also be an existing problematic for the CSM. For the PSV process, as stated previously, errors associated with any deviation from the used average particle diameter size leads to measurement inaccuracies. As reported in Fig. 12, a single square pixel has a size of 0.0556 mm, which would lead to a particle diameter precision of ± 27.5 μm. Additionally, the velocity precision obtained through the PSV method is also highly dependent on the IR camera pixel resolution, as illustrated in Fig. 12, which would result in a velocity precision of ± 5.5 m/s.

Fig. 13 Comparison between particle velocity measurements obtained using the IR camera and the CSM at stagnation temperatures of 200 and 500 °C. Median values for all three tests are provided directly on the graph

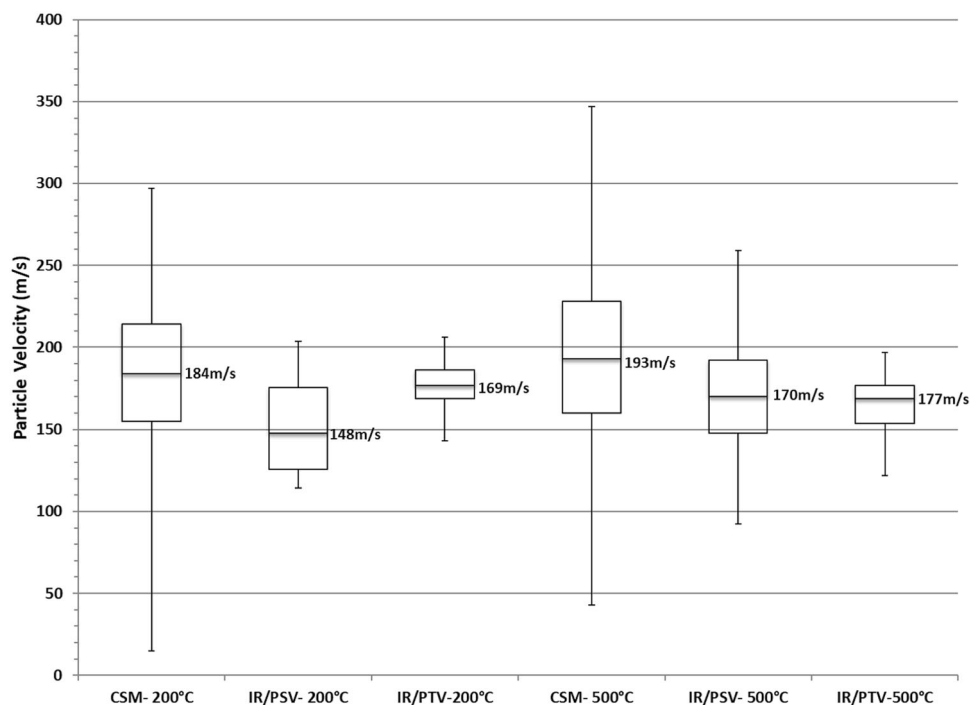
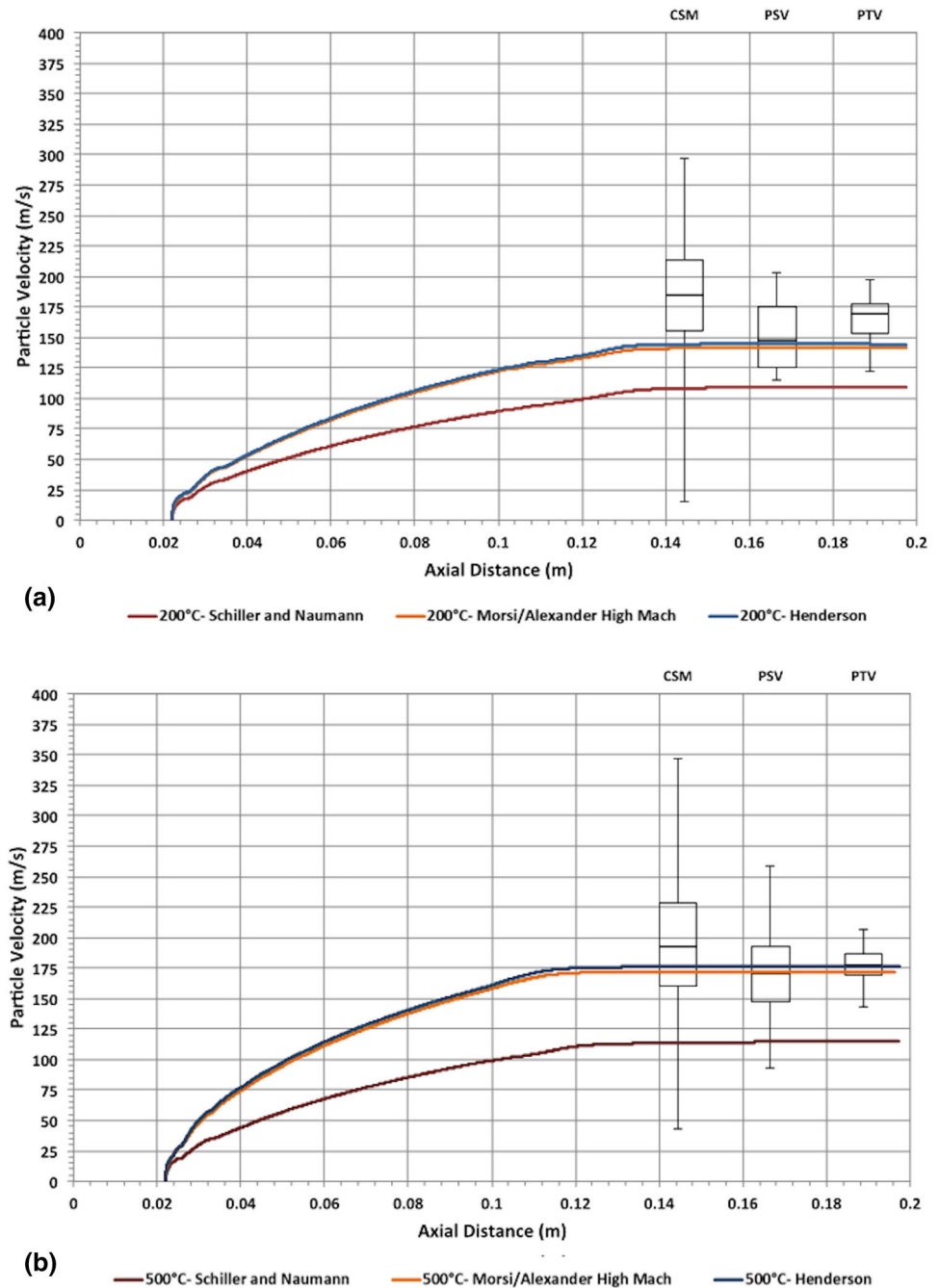


Fig. 14 Drag coefficient equation confirmation by comparison with particle experimental velocity measurements

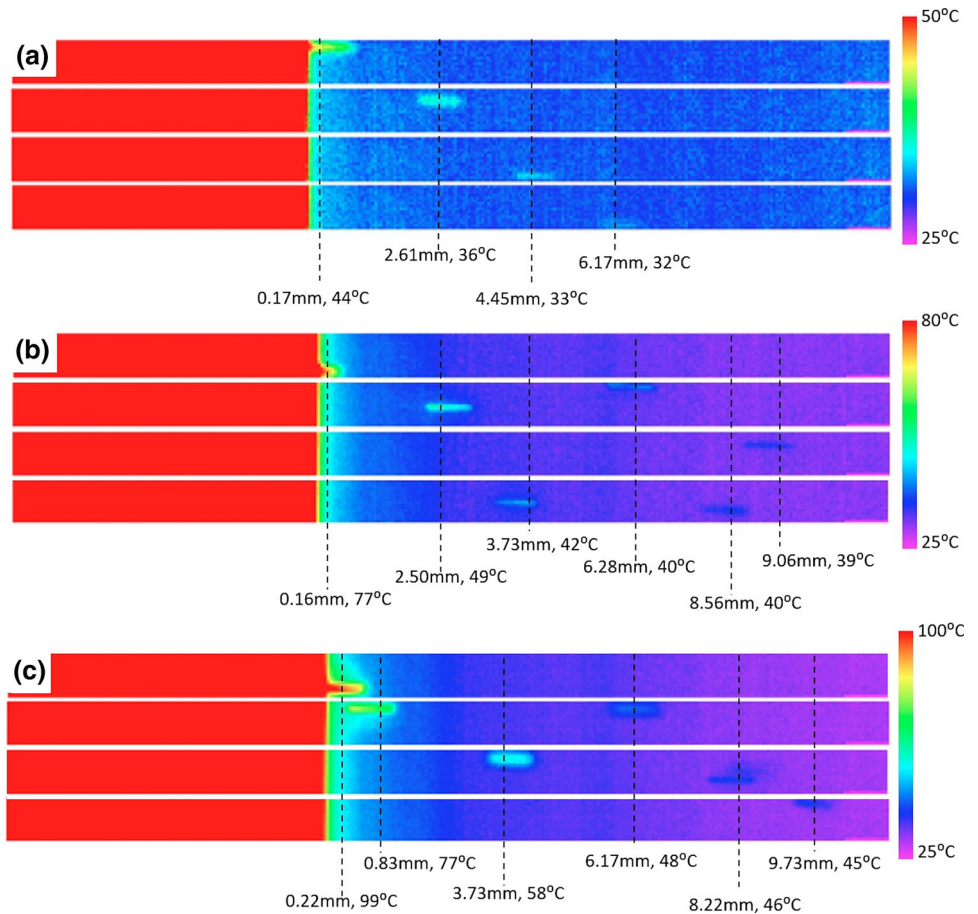


Numerical Results

The momentum transfer from the CS nitrogen flow to the titanium particles is dependent on the drag coefficient, as described previously. Figure 14 gives the simulated particle velocity from the injection point up to the end of the numerical domain boundary at 0.20 m for three different drag coefficients at stagnation temperatures of 200 and 500 °C. Experimental results obtained using all three particle velocity measurement procedures have been used to

validate the drag coefficient relation for the current flow simulation and consequently the CFD model description. The drag described by Schiller and Naumann (Eq 10), which is already implemented in the Fluent interface, leads to the lowest particle velocity. The model is derived from experimental data and provides means of calculating particle velocity for Re_p number ranging between 10^{-3} and 10^4 . However, it lacks to include the influence of the particle M_p and as a consequence the velocities obtained are 107 and 115 m/s for tests conducted using a stagnation

Fig. 15 Particle temperature measurement after the nozzle exit during CS at a stagnation temperature of (a) 200 °C, (b) 400 °C and (c) 500 °C. Individual particle location and temperature within the gas flow at the nozzle exit are provided



temperature of 200 and 500 °C, respectively. The second tested C_D correlation is also included in Fluent and is based on the correlation given by Morsi and Alexander that integrates a correction factor to account for a M_p greater than 0.4 (Eq 11). The obtained velocities are much higher than the ones resulting from the Schiller and Naumann and as a result are much closer to the experimental values. For gas stagnation of 200 and 500 °C, the simulated resulting velocities are 141 and 173 m/s, respectively. The last correlation given by Henderson, which is presented in detail in “Particle Motion” section, has been implemented separately through a user-defined function (UDF). Values attained are similar to results obtained with the drag coefficient correlation developed by Morsi and Alexander. Simulated particle velocity values reach 145 and 176 m/s for inlet gas temperature of 200 and 500 °C, respectively. Both correlations that include the influence of the relative Mach number provide an acceptable particle speed value when compared to experimental results. Consequently, the necessity to use a C_D coupled with the M_p values is of utmost importance. Additionally, based on results presented in Fig. 14, the PSV method seems to provide the most accurate and precise particle velocity reading. The

large data deviation in the CSM particle velocity results lowers its precision and consequently prohibits any direct comparison to be made with the CFD calculated values since a velocity value for a single particle diameter is sought in the current study.

Furthermore, the particle velocity stays constant throughout its travel in the CS plume although the gas reaches speed values below particle velocity. The higher mass and consequently larger inertia of the titanium particles used in the current study hinder rapid particle deceleration although the gas velocity reaches values as low as 75 m/s for both tested gas stagnation temperatures at a position of 0.18 m.

Particle Temperature

Experimental Measurements Analysis and Effect of Nozzle Reflected Temperature

During particle temperature measurements, few particles have been simultaneously observed in a single frame due to the low selected feeding rate, as shown in Fig. 15. For all cases, the highest recorded particle temperature is measured

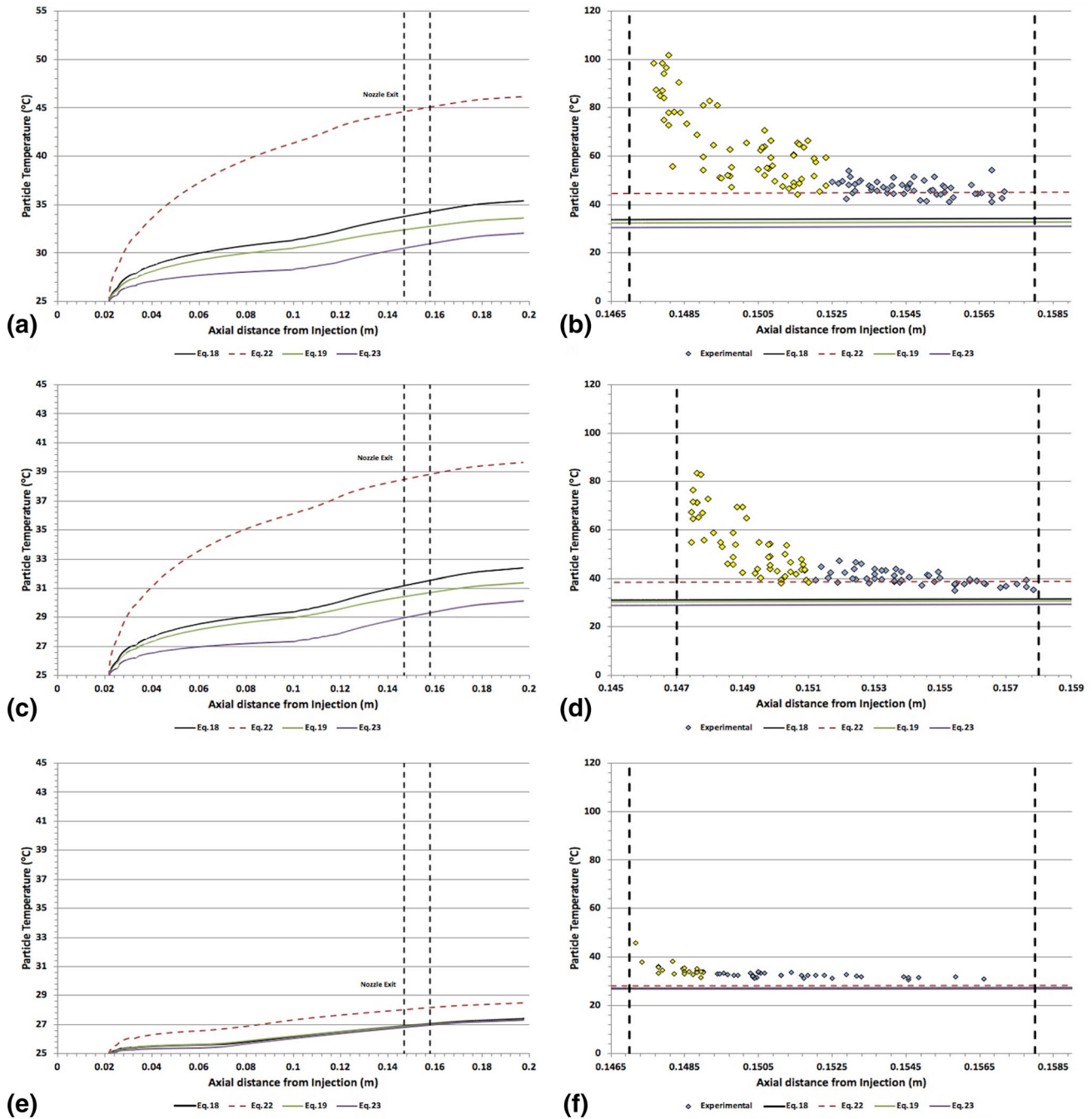


Fig. 16 For gas stagnation temperatures of 500 °C (a, b), 400 °C (c, d) and 200 °C (e, f), the particle simulated and measured temperatures after the nozzle exit are provided. Dotted lines indicate the region analyzed using the IR camera. Plots on the left (a, c, and e) show the general trend of simulated particle temperature after injection

near the nozzle exit with approximate values of 44, 77 and 99 °C for gas stagnation temperatures of 200, 400 and 500 °C, respectively. These temperatures are decreasing until reaching a constant value in the observation zone after a distance that is function of the stagnation temperature, as shown in Fig. 15. These constant temperature values reach 32, 39 and 45 °C at a gas stagnation temperature of 200, 400

and 500 °C, respectively. The measured decreasing particle temperature trend is physically impossible as the simulated gas temperature remains at a constant and higher temperature than the particle surface throughout the experimentally visible section, as shown in Fig. 9.

To explain the decreasing particle temperature process from the exit to the near nozzle exit region of the zone

observed using the IR camera, the concept of reflected temperature is used. The notion of reflected temperature is based on the effect of steel nozzle wall temperature onto the particle reflected energy. The closer the particle is to the exit, the higher is the effect of reflection from the nozzle. However, due to the CS process nature, i.e., high-speed and high-temperature exit gas flow and particle surface size, the measurement of reflected temperature from the nozzle onto the particle surface is particularly difficult to measure. Hence, in the current study, this measurement has been omitted and particle temperature readings obtained far from the nozzle exit have been taken as representative and accurate of the particle current temperature. In accordance with Eq 31, particles found near the nozzle exit experience a high T_{ref} value, which increases the signal detected by the IR camera from the in-flight particles. As stated, since the reflected temperature value is hard to measure, the true particle temperature, T_p , is consequently hard to evaluate. However, it is expected that particles found far enough from the nozzle exit experience a room temperature T_{ref} , making it possible to obtain a reading of particle temperature, T_p , value with higher precision. As a result, temperatures measured for particles found far from the nozzle exit are considered to be representative of the true particle temperature.

Verification of Nusselt Number

Figure 16 provides a summary of the obtained simulated particle temperature using all four tested Nusselt correlations in comparison with measured temperatures obtained in the zone observed using the IR camera. The particle in-flight temperature within the nozzle as well as through the exit ambient region is provided for the simulated cases. For all cases, the particle temperature continuously increases following the curves depicted in Fig. 16. Additionally, for all cases and outside the nozzle reflection affected zone, as depicted in Fig. 16(b), (d) and (f), the simulated temperature is constant (increase of 0.1%) throughout the entire section analyzed experimentally using the IR camera. Figure 16(a) shows the predicted particle temperature from their injection location to the end of the computation domain for a gas stagnation temperature of 500 °C. The Nusselt correlation given by Eq 18, and used by many in the CS field, predicts a temperature of 34 °C in the region analyzed by the IR camera, while this value reaches 33 and 31 °C using Eq 19 and 23, respectively. Moreover, the Nusselt correlation described by Eq 22 gives a higher predicted temperature of 45 °C. This predicted value falls quite precisely onto the experimentally obtained results, as shown in Fig. 16(b).

Similarly, for the spray conducted at a stagnation temperature of 400 °C, the predicted particle temperature

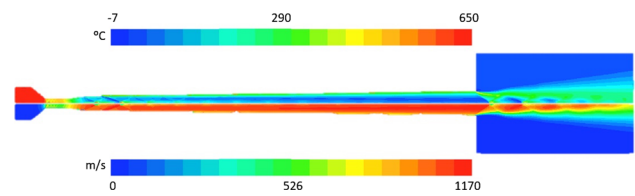


Fig. 17 High stagnation parameter spray (3.45 MPa, 650 °C) resulting flow temperature (top) and velocity (bottom) inside and outside the nozzle

increases throughout their flight within and outside the nozzle, to reach values of 31, 31 °C and 29 °C using Eq 18, 19 and 23, respectively in the experimentally observed zone. Once again, the temperature corresponding more closely to the measured value is obtained using Eq 22 with a resulting value of 39 °C. Analogously, the spray produced at an inlet stagnation temperature of 200 °C results in predicted temperatures at the analyzed zone of 27 °C with the use of Eq 18, 19 and 23. The temperature obtained using Eq 22, which has been demonstrated to be reasonably in agreement with measured temperature values for sprays conducted at higher stagnation values, results in a particle predicted temperature of 28 °C. Consequently, a difference of 4 °C is observed between predicted and measured particle values for this case. This difference can be attributed to temperature evaluation difficulties caused by the small temperature difference between background and particles. As depicted in Fig. 15(a), particles are barely seen after a distance of 6.17 mm from the nozzle outlet when using the shown scale.

Additionally, from Fig. 16(a), (c) and (e), it is seen that a similar increasing particle temperature trend is observed for all tested gas stagnation temperatures. As the particle is injected, its temperature increases sharply as it comes in contact with a low-speed high-temperature flow after the nozzle throat. During its flight in the progressively accelerating flow, the particle temperature increases rate gradually declines.

The effect of emissivity on measured temperature and the influence of particle diameter size on the simulated particle temperature have been evaluated. The emissivity has been varied from $\varepsilon = 0.40$ to $\varepsilon = 0.85$ for measured values, and the particle temperature for titanium powder with a diameter of 125 μm has been simulated for all cases using the generated model. The chosen diameter represents the smallest titanium particle obtained after the sieving process. The simulated particle temperature has indicated an increase in surface temperature with a decrease in particle diameter. Similarly, decreasing the emissivity has increased the particle observed temperature. In general, results have shown that both parameters induce differences of less than 3% with current values and as such lead to the same conclusion that the Nusselt correlation expressed by

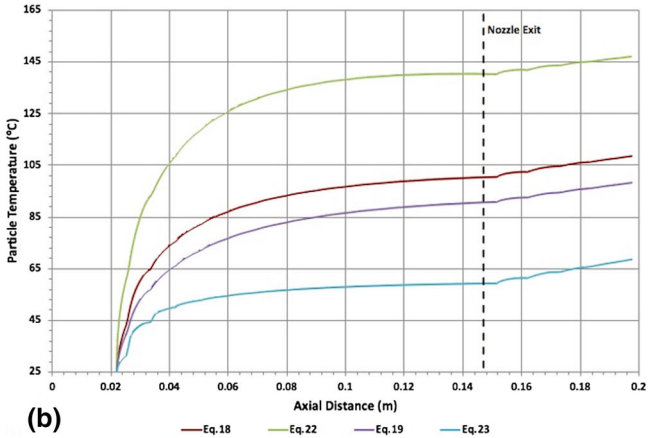
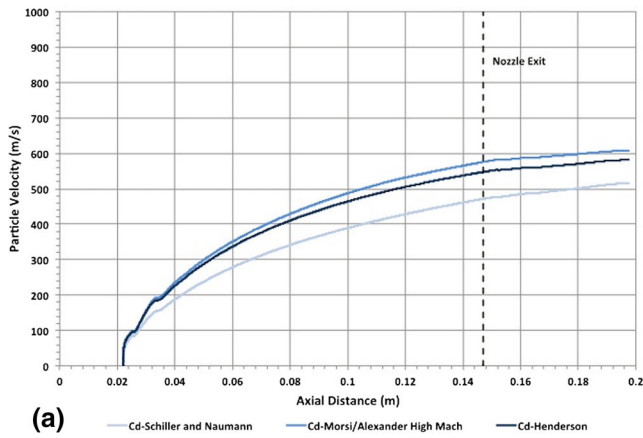


Fig. 18 Copper particle with 15 μm diameter (a) velocity and (b) temperature after being injected in a downstream fashion. Velocity results using various drag coefficient correlations are given.

Particle temperature obtained using different Nusselt expressions is also provided. For temperature calculations, the particle velocity was predicted using the Henderson drag correlation

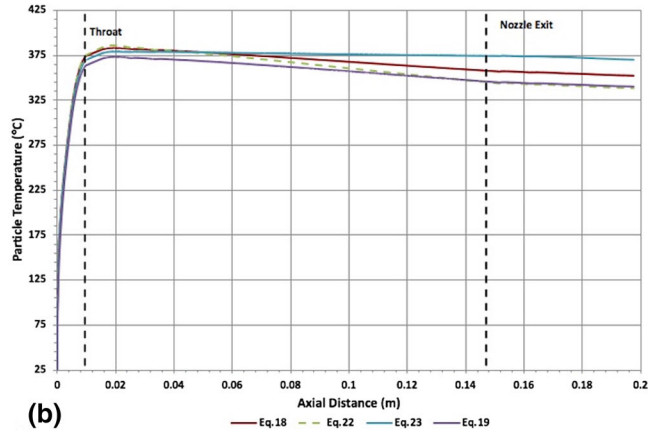
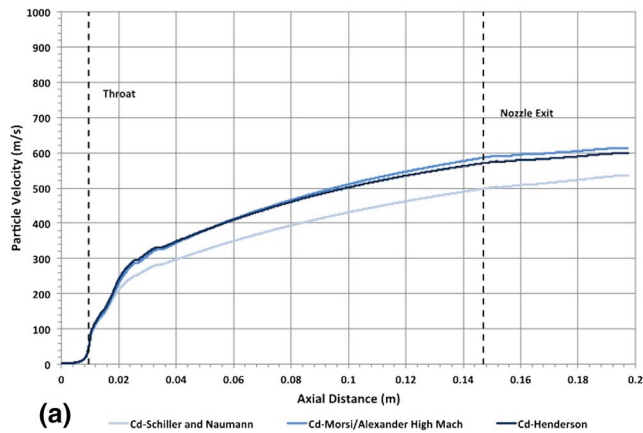


Fig. 19 Copper particle with 15 μm diameter (a) velocity and (b) temperature after being injected in an upstream fashion. Results using different drag coefficient and Nusselt correlations are given.

Particle temperature has been obtained using the velocity predicted by the Henderson drag correlation

Eq 22 provides the most accurate numerical particle temperature estimate. In addition, these results also support that any inaccuracy in the emissivity value ($\epsilon = 0.71$) leads to minor changes in resulting particle temperatures and the influence is inconsequential on the drawn conclusions.

High Pressure and Temperature Flow

Figure 17 shows the resulting gas temperature and velocity within the nozzle and at the free jet location for a gas stagnation pressure and temperature of 3.45 MPa and 650 °C, respectively. As mentioned previously, these parameters have been selected to give insight into the influence of particle/flow correlations for high deposition efficiency CS processes. A maximal gas velocity and temperature of 1093 m/s and 61 °C, respectively, are

reached at the nozzle exit. As expected, due to the nozzle geometry, an internal shock is still present after the nozzle throat. At the exit, the flow is over-expanded as a pressure of approximately 50 kPa is reached prior to the exit in the atmospheric region. Spherical copper particle with a diameter of 15 μm has been injected in the flow in an upstream and downstream position of the nozzle throat. The following sections present the results for downstream and upstream powder injections.

Downstream Particle Injection Figure 18(a) shows the copper particle velocity after injection in the high-speed flow using different drag coefficient correlations. An exit velocity of 471, 546 and 574 m/s is obtained using the Schiller and Naumann (Eq 10), Henderson (Eq 6 to 9) and Morsi and Alexander (Eq 11) correlations, respectively.

Similarly to previous low stagnation pressure simulations, the obtained particle velocities calculated using all three correlations give different results whether or not the particle Mach number is considered.

Figure 18(b) provides the particle temperature predicted by all four tested Nusselt number correlations using the particle velocity calculated through Henderson drag law. An exit particle temperature with values of 59, 91, 100 and 140 °C is predicted by correlations expressed using Eq 23, 19, 18 and 22, respectively. A difference of 81 °C (20%) is obtained between the lowest and highest, confirmed formerly to be the most accurate, predicted copper particle temperatures at the nozzle exit. All four Nusselt correlations predict a steeper increase in particle temperature after their exit from the nozzle due to the presence of the external shock waves. Particle heating is promoted in a gas flow of highly varying properties such as through shock waves.

Upstream Particle Injection Figure 19(a) gives the copper particle velocity when injected upstream on the nozzle axis in the converging section, as shown in Fig. 7. The particle slowly accelerates to low speeds in the converging section prior to the nozzle throat. Once propelled in the diverging high-speed nozzle section, the velocity of the particle increases to reach exit speeds of 494, 570 and 585 m/s using the drag coefficient given by Schiller and Naumann (Eq 10), Henderson (Eq 6 to 9) and Morsi and Alexander (Eq 11), respectively. Correlations given by Henderson as well as Morsi and Alexander provide reasonably the same particle velocity values within the nozzle up to 0.08 m. However, slight divergence in particle velocity using the two M_p dependent drag coefficient correlations is observed after 0.08 m. Results from the Henderson correlation have been taken as representative of the true particle velocity.

Figure 19(b) shows the copper particle temperature variation within the nozzle and at the exit. The particle temperature sharply increases in the hot converging inlet nozzle region to values close to 382 °C for all tested Nusselt expressions as one would expect since this region does not exhibit large compressibility effect as it is mostly low subsonic flow regime. Once in the diverging section, the particle temperature decreases to 346 °C at the nozzle exit when using both Eq 19 and 22. This value, however, reaches 356 °C and 374 °C when using the Nusselt correlation expressed by Eq 18 and 23, respectively. As seen in Fig. 19(b), the correlation expressed by Eq 19 provides the same accuracy as Eq 22, which has been asserted most accurate from previous results. The gas flow temperature and Mach number at the exit reach values of approximately 61 °C and 3, respectively. Although the gas reaches low temperatures as it expands in the diverging section, the

particle high velocity allows only an approximate 50 °C of temperature drop to occur, as shown in Fig. 19(b).

Conclusions

Newly available infrared camera with high spatial resolution along with fast readout speed has allowed obtaining the first particle temperature measurement in the CS field. However, the IR camera used is limited to a wavelength range of 3 to 5 μm . This is not ideal for low temperature readings, as the radiation at low temperatures is easier to detect at longer wavelengths. Additionally, although the exposure time of the used IR camera is considered very small, lower exposure times would lead to clearer and higher detection rates. This also limits the velocity at which particles can travel, in order to be properly detected by the camera without any large streak, to a few hundred m/s and limits the number of particles detected per optical window. Although the resolution is high, small particles of 30 μm , more generally used in the CS field, would not be perceivable with the current IR camera as the resolution consists of pixels with 55 μm size.

Nevertheless, measurements of CS particle temperature have been successfully achieved for 150 μm titanium particles injected downstream in the cold spray gas flow. Results of particle temperature at the nozzle exit vicinity for various gas inlet temperatures were obtained and compared to measured particle temperatures. Evaluation of Nusselt number correlations for heat transfer analysis provided that the following equation is most accurate in predicting the particle temperature;

$$\overline{Nu} = 2 + 0.44Re_p^{0.5}Pr^{0.33} \exp(0.1 + 0.872M_p)$$

Using other correlations can lead to considerable particle temperature differences. These differences can lead to incorrect particle to substrate impact behavior during impact modeling, which has been significantly used in the CS community to provide insight to the impact phenomenon and material deformation processes. Hence, the current study has provided insight with regard to the most appropriate Nusselt correlation to use when modeling CS particles.

In addition, the IR camera has also been utilized as an additional tool for particle in-flight velocity measurement. As the testing process provides visual data of particles during their flight at the exit of the nozzle and up to a standoff distance of approximately 11 mm, particle tracking velocimetry and particle streak velocimetry methods have been used to obtain readings of velocity. Results have been compared to values measured using the commercial Cold Spray Meter equipment. All three measuring techniques validate the accuracy of the Henderson drag law correlation in predicting particle velocity. The particle

streak velocimetry has shown that in addition to providing local particle size and location, it can be utilized to measure individual particle velocity at specific location within the flow. The PSV method has shown to provide the most accurate particle velocity range compared to the CSM and particle tracking velocimetry based on numerically calculated velocity values for 150 μm diameter particles.

With continuously developing technology, the current work provides foundation to future studies that could potentially be made using more advanced IR camera to provide particle temperature readings for any particle diameter traveling at any velocity commonly found in the CS process.

Acknowledgments The authors wish to thank Vincent Farley and Karl-Alexandre Jahjah from Telops Inc. for providing the necessary equipment for temperature measurement used in the current study and for their input into the data analysis process.

Appendix A

The drag coefficients from Eq 11 for various Re_p numbers are given as follows;

$$C_D = \frac{24.0}{Re_p} \quad \text{for } 0 < Re_p < 0.1,$$

$$C_D = 3.69 + \frac{22.73}{Re_p} + \frac{0.0903}{Re_p^2} \quad \text{for } 0.1 < Re_p < 1$$

$$C_D = 1.222 + \frac{29.1667}{Re_p} - \frac{3.8889}{Re_p^2} \quad \text{for } 1 < Re_p < 10,$$

$$C_D = 0.6167 + \frac{46.50}{Re_p} - \frac{116.67}{Re_p^2} \quad \text{for } 10 < Re_p < 100$$

$$C_D = 0.3644 + \frac{98.33}{Re_p} - \frac{2778}{Re_p^2} \quad \text{for } 100 < Re_p < 1000$$

$$C_D = 0.357 + \frac{148.62}{Re_p} - \frac{47500}{Re_p^2} \quad \text{for } 1000 < Re_p < 5000$$

$$C_D = 0.46 - \frac{490.546}{Re_p} - \frac{57.87 \times 10^4}{Re_p^2} \quad \text{for } 5000 < Re_p < 10000$$

$$C_D = 0.5191 - \frac{1662.5}{Re_p} - \frac{5.4167 \times 10^6}{Re_p^2} \quad \text{for } Re_p \geq 10,000$$

References

1. B. Jodoin, Cold Spray Nozzle Mach Number Limitation, *J. Therm. Spray Technol.*, 2002, **11**(4), p 496-507
2. W.-Y. Li, C. Zhang, C.-J. Li, and H. Liao, Modeling Aspects of High Velocity Impact of Particles in Cold Spraying by Explicit Finite Element Analysis, *J. Therm. Spray Technol.*, 2009, **18**(5-6), p 921-933
3. T. Schmidt, H. Assadi, F. Gartner, H. Richter, T. Stoltenhoff, H. Kreye, and T. Klassen, From Particle Acceleration to Impact and Bonding in Cold Spraying, *J. Therm. Spray Technol.*, 2009, **18**(5-6), p 794-808
4. A.E. Segall, A.N. Papyrin, J.C. Conway, and D. Shapiro, A Cold-Gas Spray Coating Process for Enhancing Titanium, *JOM J. Miner. Met. Mater. Soc.*, 1998, **50**, p 52-54
5. T. Stoltenhoff, H. Kreye, and H.J. Richter, An Analysis of the Cold Spray Process and Its Coatings, *J. Therm. Spray Technol.*, 2002, **11**(4), p 542-550
6. R. Kapoor and S. Nemat-Nasser, Determination of Temperature Rise during High Strain Rate Deformation, *Mech. Mater.*, 1998, **27**(1), p 1-12
7. J. Manson, A. Rosakis, and G. Ravichandran, On the Strain and Strain Rate Dependence of the Fraction of Plastic Work Converted to Heat: An Experimental Study Using High Speed Infrared Detectors and the Kolsky Bar, *Mech. Mater.*, 1994, **17**(2-3), p 135-145
8. T. Børvik, O.S. Hopperstad, T. Berstad, and M. Langseth, Perforation of 12 Mm Thick Steel Plates by 20 Mm Diameter Projectiles with Flat, Hemispherical and Conical Noses: Part II: Numerical Simulations, *Int. J. Impact Eng.*, 2002, **27**(1), p 37-64
9. S. Yin, X. Wang, W. Li, and X. Guo, Examination on Substrate Preheating Process in Cold Gas Dynamic Spraying, *J. Therm. Spray Technol.*, 2011, **20**(4), p 852-859
10. A.G. McDonald, A.N. Ryabinin, E. Irissou, and J.-G. Legoux, Gas-Substrate Heat Exchange During Cold-Gas Dynamic Spraying, *J. Therm. Spray Technol.*, 2013, **22**(2-3), p 391-397
11. J.G. Legoux, E. Irissou, and C. Moreau, Effect of Substrate Temperature on the Formation Mechanism of Cold-Sprayed Aluminum, Zinc and Tin Coatings, *J. Therm. Spray Technol.*, 2007, **16**(5-6), p 619-626
12. W.-Y. Li, H. Liao, G. Douchy, and C. Coddet, Optimal Design of a Cold Spray Nozzle by Numerical Analysis of Particle Velocity and Experimental Validation with 316L Stainless Steel Powder, *Mater. Des.*, 2007, **28**(7), p 2129-2137
13. M.-W. Lee, J.-J. Park, D.-Y. Kim, S.S. Yoon, H.-Y. Kim, S.C. James, S. Chandra, and T. Coyle, Numerical Studies on the Effects of Stagnation Pressure and Temperature on Supersonic Flow Characteristics in Cold Spray Applications, *J. Therm. Spray Technol.*, 2011, **20**(5), p 1085-1097
14. A. Sova, A. Okunkova, S. Grigoriev, and I. Smurov, Velocity of the Particles Accelerated by a Cold Spray Micronozzle: Experimental Measurements and Numerical Simulation, *J. Therm. Spray Technol.*, 2012, **22**(1), p 2013-2075
15. R. Ghelichi, S. Bagherifard, M. Guagliano, and M. Verani, Numerical Simulation of Cold Spray Coating, *Surf. Coat. Technol.*, 2011, **205**, p 5294-5301
16. M. Karimi, A. Fartaj, G. Rankin, D. Vanderzwet, W. Birtch, and J. Villafuerte, Numerical Simulation of the Cold Gas Dynamic Spray Process, *J. Therm. Spray Technol.*, 2006, **15**(4), p 518-523

17. W.-Y. Li, H. Liao, H.-T. Wang, C.-J. Li, G. Zhang, and C. Coddet, Optimal Design of a Convergent-Barrel Cold Spray Nozzle by Numerical Method, *Appl. Surf. Sci.*, 2006, **253**(2), p 708-713
18. S. Yin, M. Meyer, W. Li, H. Liao, and R. Lupoi, Gas Flow, Particle Acceleration, and Heat Transfer in Cold Spray: A Review, *J. Therm. Spray Technol.*, 2016, **25**(5), p 874-896
19. H. Assadi, T. Schmidt, H. Richter, J.-O. Kliemann, K. Binder, F. Gärtner, T. Klassen, and H. Kreye, On Parameter Selection in Cold Spraying, *J. Therm. Spray Technol.*, 2011, **20**(6), p 1161-1176
20. A.P. Alkhimov, V.F. Kosarev, and S.V. Klinkov, The Features of Cold Spray Nozzle Design, *J. Therm. Spray Technol.*, 2001, **10**(2), p 375-381
21. V.F. Kosarev, S.V. Klinkov, A.P. Alkhimov, and A.N. Papyrin, On Some Aspects of Gas Dynamics of the Cold Spray Process, *J. Therm. Spray Technol.*, 2003, **12**(2), p 265-281
22. B. Samareh, O. Stier, V. Lüthen, and A. Dolatabadi, Assessment of CFD Modeling via Flow Visualization in Cold Spray Process, *J. Therm. Spray Technol.*, 2009, **18**(5-6), p 934-943
23. D.L. Gilmore, R.C. Dykhuizen, R.A. Neiser, M.F. Smith, and T.J. Roemer, Particle Velocity and Deposition Efficiency in the Cold Spray Process, *J. Therm. Spray Technol.*, 1999, **8**(4), p 576-582
24. B. Jodoin, F. Raletz, and M. Vardelle, Cold Spray Modeling and Validation Using an Optical Diagnostic Method, *Surf. Coat. Technol.*, 2006, **200**(14-15), p 4424-4432
25. V.K. Champagne, D.J. Helfritsch, S.P.G. Dinavahi, and P.F. Leyman, Theoretical and Experimental Particle Velocity in Cold Spray, *J. Therm. Spray Technol.*, 2011, **20**(3), p 425-431
26. S.P. Mates, D. Basak, F.S. Biancanello, S.D. Ridder, and J. Geist, Calibration of a Two-Color Imaging Pyrometer and Its Use for Particle Measurements in Controlled Air Plasma Spray Experiments, *J. Therm. Spray Technol.*, 2002, **11**(2), p 195-205
27. G. Mauer, R. Vaßen, and D. Stöver, Plasma and Particle Temperature Measurements in Thermal Spray: Approaches and Applications, *J. Therm. Spray Technol.*, 2011, **20**(3), p 391-406
28. B. Aziz, P. Gougeon, and C. Moreau, Temperature Measurement Challenges and Limitations for In-Flight Particles in Suspension Plasma Spraying, *J. Therm. Spray Technol.*, 2017, **26**(4), p 695-707
29. J. Vattulainen, E. Hämäläinen, R. Hernberg, P. Vuoristo, and T. Mäntylä, Novel Method for In-Flight Particle Temperature and Velocity Measurements in Plasma Spraying Using a Single CCD Camera, *J. Therm. Spray Technol.*, 2001, **10**(1), p 94-104
30. T.C. Hanson, C.M. Hackett, and G.S. Settles, Independent Control of HVOF Particle Velocity and Temperature, *J. Therm. Spray Technol.*, 2002, **11**(1), p 75-85
31. B.H. Wang, B.Q. Li, H. Yang, and Y. Bai, Radiation Spectral Analysis and Particle Temperature/Velocity Measurement in Plasma Spray with One-Color Camera, *J. Therm. Spray Technol.*, 2017, **26**(7), p 1632-1640
32. J. Mishin, M. Vardelle, J. Lesinski, and P. Fauchais, Two-Colour Pyrometer for the Statistical Measurement of the Surface Temperature of Particles under Thermal Plasma Conditions, *J. Phys. E*, 1987, **20**(6), p 620-625
33. K. Hollis and R. Neiser, Particle Temperature and Flux Measurement Utilizing a Nonthermal Signal Correction Process, *J. Therm. Spray Technol.*, 1998, **7**(3), p 392-402
34. P. Fauchais and M. Vardelle, Sensors in Spray Processes, *J. Therm. Spray Technol.*, 2010, **19**(4), p 668-694
35. G.A. Hughmark, Mass and Heat Transfer from Rigid Sphere, *AIChE J.*, 1967, **13**(6), p 1219-1221
36. D.J. Carlson and R.F. Hoglund, Particle Drag and Heat Transfer in Rocket Nozzles, *AIAA J.*, 1964, **2**(11), p 1980-1984
37. Y.P. Wan, V. Prasad, G.-X. Wang, S. Sampath, and J.R. Fincke, Model and Powder Particle Heating, Melting, Resolidification, and Evaporation in Plasma Spraying Processes, *J. Heat Transf.*, 1999, **121**(3), p 691-699
38. T.-C. Jen, L. Pan, L. Li, Q. Chen, and W. Cui, The Acceleration of Charged Nano-Particles in Gas Stream of Supersonic de-Laval-Type Nozzle Coupled with Static Electric Field. *Appl. Therm. Eng.*, 2006, **26**(5-6), 613-621
39. H. Tabbara, S. Gu, D.G. McCartney, T.S. Price, and P.H. Shipway, Study on Process Optimization of Cold Gas Spraying, *J. Therm. Spray Technol.*, 2011, **20**(3), p 608-620
40. T. Jen, L. Li, W. Cui, Q. Chen, and X. Zhang, Numerical Investigations on Cold Gas Dynamic Spray Process with Nano- and Microsize Particles, *Int. J. Heat Mass Transf.*, 2005, **48**(21-22), p 4384-4396
41. M. Faizan-Ur-Rab, S.H. Zahiri, S.H. Masood, T.D. Phan, M. Jahedi, and R. Nagarajah, Application of a Holistic 3D Model to Estimate State of Cold Spray Titanium Particles, *Mater. Des.*, 2016, **89**, p 1227-1241
42. G. Huang, D. Gu, X. Li, L. Xing, and H. Wang, Numerical Simulation on Syphonage Effect of Laval Nozzle for Low Pressure Cold Spray System, *J. Mater. Process. Technol.*, 2014, **214**(11), p 2497-2504
43. X.K. Suo, T.K. Liu, W.Y. Li, Q.L. Suo, M.P. Planche, and H.L. Liao, Numerical Study on the Effect of Nozzle Dimension on Particle Distribution in Cold Spraying, *Surf. Coat. Technol.*, 2013, **220**, p 107-111
44. D.-M. Chun, J.-O. Choi, C.S. Lee, and S.-H. Ahn, Effect of Stand-off Distance for Cold Gas Spraying of Fine Ceramic Particles (5 μm) under Low Vacuum and Room Temperature Using Nano-Particle Deposition System (NPDS), *Surf. Coat. Technol.*, 2012, **206**, p 2125-2132
45. S. Yin, M. Zhang, Z. Guo, H. Liao, and X. Wang, Numerical Investigations on the Effect of Total Pressure and Nozzle Divergent Length on the Flow Character and Particle Impact Velocity in Cold Spraying, *Surf. Coat. Technol.*, 2013, **232**, p 290-297
46. J. Pattison, S. Celotto, A. Khan, and W. O'Neill, Standoff Distance and Bow Shock Phenomena in the Cold Spray Process, *Surf. Coat. Technol.*, 2008, **202**(8), p 1443-1454
47. X. Suo, S. Yin, M.-P. Planche, T. Liu, and H. Liao, Strong Effect of Carrier Gas Species on Particle Velocity During Cold Spray Processes, *Surf. Coat. Technol.*, 2014, **268**, p 1-4
48. C.T. Crowe, J.D. Schwarzkopf, M. Sommerfeld, and Y. Tsuji, *Multiphase Flows with Droplets and Particles*, CRC Press, Boca Raton, 2011
49. M.A. Saad, *Compressible Fluid Flow*, Prentice-Hall, Englewood Cliffs, NJ, 1985
50. E. Loth, Compressibility and Rarefaction Effects on Drag of a Spherical Particle, *AIAA J.*, 2008, **46**, p 2219-2228
51. I.-S. Chang, One- and Two-Phase Nozzle Flows, *AIAA J.*, 1980, **18**(12), p 1455-1461
52. C.T. Crowe, Drag Coefficient of Particles in a Rocket Nozzle, *AIAA J.*, 1967, **5**(5), p 1021-1022
53. C.B. Henderson, Drag Coefficients of Spheres in Continuum and Rarefied Flows, *AIAA J.*, 1976, **14**(6), p 707-708
54. J. Aroesty, Sphere Drag in a Low-Density Supersonic Flow, in *Rarefied Gas Dynamics, Volume 2, Proceedings of the Third International Symposium*, (NY), Academic Press, pp. 261-277 (1963)
55. A.B. Bailey and J. Hiatt, Sphere Drag Coefficients for a Broad Range of Mach and Reynolds Numbers, *AIAA J.*, 1972, **10**(11), p 1436-1440
56. G. Mishin and G. Mishin, "Experimental Investigation of the Flight of a Sphere in Weakly Ionized Air," in *15th Applied*

- Aerodynamics Conference*, (Atlanta, GA), American Institute of Aeronautics and Astronautics, pp. 1997-2298 (1997)
57. T. Han, Z. Zhao, B.A. Gillispie, and J.R. Smith, Effects of Spray Conditions on Coating Formation by the Kinetic Spray Process, *J. Therm. Spray Technol.*, 2005, **14**(3), p 373-383
 58. S.V. Klinkov, V.F. Kosarev, A.A. Sova, and I. Smurov, Calculation of Particle Parameters for Cold Spraying of Metal-Ceramic Mixtures, *J. Therm. Spray Technol.*, 2009, **18**(5-6), p 944-956
 59. L. Talbot, R.K. Cheng, R.W. Schefer, and D.R. Willis, Thermophoresis of Particles in a Heated Boundary Layer, *J. Fluid Mech.*, 1980, **101**(4), p 737-758
 60. X.-J. Ning, Q.-S. Wang, Z. Ma, and H.-J. Kim, Numerical Study of In-Flight Particle Parameters in Low-Pressure Cold Spray Process, *J. Therm. Spray Technol.*, 2010, **19**(6), p 1211-1217
 61. S.A. Abdulaziz and A.B. Gregory, Characterization of the Interacting Gas-Particle Dynamic System in Cold Spray Nozzles in Dimensional and Non-Dimensional Form, *Powder Technol.*, 2018, **338**, p 1-47
 62. T.L. Bergman, F.P. Incropera, D.P. DeWitt, and A.S. Lavine, *Fundamentals of Heat and Mass Transfer*, Wiley, Hoboken, NJ, 2011
 63. A. Sova, M. Doubenskaia, S. Grigoriev, A. Okunkova, and I. Smurov, Parameters of the Gas-Powder Supersonic Jet in Cold Spraying Using a Mask, *J. Therm. Spray Technol.*, 2013, **22**(4), p 551-556
 64. M.P. Dewar, A.G. McDonald, and A.P. Gerlich, Interfacial Heating during Low-Pressure Cold-Gas Dynamic Spraying of Aluminum Coatings, *J. Mater. Sci.*, 2012, **47**(1), p 184-198
 65. H. Katanoda, Numerical Simulation of Temperature Uniformity within Solid Particles in Cold Spray, *J. Solid Mech. Mater. Eng.*, 2008, **2**, p 58-69
 66. B.I. Ermolaev, Thermal Conductivity and Electrical Conductivity of Materials Based on Titanium and Its Alloys at Temperatures from 20-80 to 1000°K, *Met. Sci. Heat Treat.*, 1974, **16**, p 1049-1051
 67. I.E. Beckwith and J.J. Gallagher, Heat Transfer and Recovery Temperature on a Sphere with Laminar, Transitional and Turbulent Boundary Layers at Mach Numbers of 2.00 and 4.15. Washington, (1957)
 68. S. Forrest, Survey of Literature on Convective Heat Transfer Coefficients and Recovery Factors for High Atmosphere Thermometry, Utah, USA (1973)
 69. W.E. Ranz and W.R. Marshall Jr., Evaporation from Drops Part I, *Chem. Eng. Prog.*, 1952, **48**, p 141-146
 70. V. Champagne, D. Helfritch, P. Leyman, R. Lempicki, and S. Grendahl, The Effects of Gas and Metal Characteristics on Sprayed Metal Coatings, *Model. Simul. Mater. Sci. Eng.*, 2005, **13**(7), p 1119
 71. D. Helfritch and V. Champagne Jr., A Model Study of Powder Particle Size Effects in Cold Spray Deposition, in *Proceedings of the Army Science Conference (26th)*, (Orlando), p 6 (2008)
 72. M. Faizan-Ur-Rab, S.H. Zahiri, P.C. King, C. Busch, S.H. Masood, M. Jahedi, R. Nagarajah, and S. Gulizia, Utilization of Titanium Particle Impact Location to Validate a 3D Multicomponent Model for Cold Spray Additive Manufacturing, *J. Therm. Spray Technol.*, 2017, **26**(8), p 1874-1887
 73. W.-Y. Li and C.-J. Li, Optimal Design of a Novel Cold Spray Gun Nozzle at a Limited Space, *J. Therm. Spray Technol.*, 2005, **14**(3), p 391-396
 74. E.E.S. Michaelides, *Heat and Mass Transfer in Particulate Suspensions*, Springer, Fort Worth, 2013
 75. H. Katanoda, M. Fukuhara, and N. Iino, Numerical Study of Combination Parameters for Particle Impact Velocity and Temperature in Cold Spray, *J. Therm. Spray Technol.*, 2007, **16**(5-6), p 627-633
 76. A. Aissa, M. Abdelouahab, A. Nouredine, M. El Ganaoui, and B. Pateyron, Ranz and Marshall Correlations Limits on Heat Flow Between a Sphere and Its Surrounding Gas at High Temperature, *Therm. Sci.*, 2015, **19**(5), p 1521-1528
 77. F. Ben Ettouil, B. Pateyron, H. Ageorges, M. El Ganaoui, P. Fauchais, and O. Mazhorova, Fast Modeling of Phase Changes in a Particle Injected Within a d.c Plasma Jet, *J. Therm. Spray Technol.*, 2007, **16**(5-6), p 744-750
 78. C. Borgnakke and R.E. Sonntag, *Fundamentals of Thermodynamics*, 9th ed., Wiley Global Education, Michigan, 2016
 79. T.H.V. Steenkiste, J.R. Smith, and R.E. Teets, Aluminum Coatings via Kinetic Spray with Relatively Large Powder Particles, *Surf. Coat. Technol.*, 2002, **154**(2-3), p 237-252
 80. E.H. Kwon, S.H. Cho, J.W. Han, C.H. Lee, and H.J. Kim, Particle Behavior in Supersonic Flow During the Cold Spray Process, *Met. Mater. Int.*, 2005, **11**(5), p 377-381
 81. R.C. Dykhuizen and M.F. Smith, Gas Dynamic Principles of Cold Spray, *J. Therm. Spray Technol.*, 1998, **7**(2), p 205-212
 82. P. Tremblay, L. Belhumeur, M. Chamberland, A. Villemaire, P. Dubois, F. Marcotte, C. Belzile, V. Farley, and P. Lagueux, Pixel-Wise Real-Time Advanced Calibration Method for Thermal Infrared Cameras, in *Proceedings Volume 7662, Infrared Imaging Systems: Design, Analysis, Modeling, and Testing XXI*, ed. by G.C. Holst and K.A. Krapels, Orlando, p 766212 (2010)
 83. Y. Tanida and H. Miyashiro, Flow Visualization VI, in *Proceedings of the Sixth International Symposium on Flow Visualization*, ed. by H. Tanida, Yoshimichi, Miyashiro, (Springer, Yokohama), p 904 (2013)
 84. A. Ianiro and G. Cardone, Measurement of Surface Temperature and Emissivity with Stereo Dual-Wavelength IR Thermography, *J. Mod. Opt.*, 2010, **57**(18), p 1708-1715
 85. R. Usamentiaga, P. Venegas, J. Guerediaga, L. Vega, J. Molleda, and F. Bulnes, Infrared Thermography for Temperature Measurement and Non-Destructive Testing, *Sensors*, 2014, **14**(7), p 12305-12348
 86. M.V. Möllmann, *Infrared Thermal Imaging: Fundamentals, Research and Applications*, 2nd ed., Wiley-VCH, Weinheim, 2017
 87. T.K. Bose, *High Temperature Gas Dynamics: An Introduction for Physicists and Engineers*, 2nd ed., Springer, Kolkata, West Bengal, 2014
 88. M. Ochs, T. Horbach, A. Schulz, R. Koch, and H.J. Bauer, A Novel Calibration Method for an Infrared Thermography System Applied to Heat Transfer Experiments, *Meas. Sci. Technol.*, 2009, **20**(7), p 1-9
 89. G.M. Carlomagno and G. Cardone, Infrared Thermography for Convective Heat Transfer Measurements, *Exp. Fluids*, 2010, **49**(6), p 1187-1218
 90. N.K. Tolochko, Y.V. Khlopkov, S.E. Mozzharov, M.B. Ignatiev, T. Laoui, and V.I. Titov, Absorptance of Powder Materials Suitable for Laser Sintering, *Rapid Prototyp. J.*, 2000, **6**(3), p 155-161
 91. Y. Li and D. Gu, Thermal Behavior during Selective Laser Melting of Commercially Pure Titanium Powder: Numerical Simulation and Experimental Study, *Addit. Manuf.*, 2014, **1-4**, p 99-109
 92. N.K. Tolochko, M.K. Arshinov, A.V. Gusarov, V.I. Titov, T. Laoui, and L. Froyen, Mechanisms of Selective Laser Sintering and Heat Transfer in Ti Powder, *Rapid Prototyp. J.*, 2003, **9**(5), p 314-326
 93. F. Zhang, K. Yu, K. Zhang, Y. Liu, Y. Zhao, and Y. Liu, Infrared Spectral Emissivity Property of Pure Titanium in the 473-1035 K Temperature Range, *Appl. Spectrosc.*, 2016, **70**(10), p 1717-1725
 94. Z.W. Wang, Y.M. Wang, Y. Liu, J.L. Xu, L.X. Guo, Y. Zhou, J.H. Ouyang, and J.M. Dai, Microstructure and Infrared

- Emissivity Property of Coating Containing TiO₂ Formed on Titanium Alloy by Microarc Oxidation, *Curr. Appl. Phys.*, 2011, **11**(6), p 1405-1409
95. G. Teodorescu, P.D. Jones, R.A. Overfelt, and B. Guo, High Temperature Emissivity of High Purity Titanium and Zirconium, (Alabama) (2018)
96. E.A. Belskaya, Emissivity and Electrical Resistivity of Titanium Alloys with Aluminum and Vanadium, *High Temp.*, 2012, **50**(4), p 475-478
97. F.J. Bradshaw, The Optical Emissivity of Titanium and Zirconium, *Proc. Phys. Soc. Sect. B*, 1950, **63**(8), p 573
98. J.M. Jones, P. Mason, and A. Williams, A Compilation Of Data On The Radiant Emissivity Of Some Materials At High Temperatures. J. Energy Inst. (2018) (in press)
99. M.F. Modest, *Radiative Heat Transfer*, 3rd ed., Academic Press, Amsterdam, 2013
100. B. Lane, S. Moylan, E. Whinton, and L. Ma, Thermographic Measurements of the Commercial Laser Powder Bed Fusion Process at NIST, *Rapid Prototyp. J.*, 2016, **22**(5), p 778-787
101. S.H. Zahiri, T.D. Phan, S.H. Masood, and M. Jahedi, Development of Holistic Three-Dimensional Models for Cold Spray Supersonic Jet, *J. Therm. Spray Technol.*, 2014, **23**(6), p 919-933
102. B. Samareh and A. Dolatabadi, Dense Particulate Flow in a Cold Gas Dynamic Spray System, *J. Fluids Eng.*, 2008, **130**(8), p 1-11